Disposition of Nirmatrelvir, an Orally Bioavailable Inhibitor of SARS-CoV-2 3C-Like Protease, across Animals and Humans[S]

Heather Eng, Alyssa L. Dantonio, Eugene P. Kadar, R. Scott Obach, Li Di, Jian Lin,
Nandini C. Patel, Britton Boras, Gregory S. Walker, Jonathan J. Novak,[1] Emi Kimoto,
Ravi Shankar P. Singh and Amit S. Kalgutkar

Pfizer Worldwide Research, Development, and Medical, Groton, Connecticut (H.E., A.L.D., E.P.K., R.S.O., L.D., J.L., G.S.W., J.J.N., E.K.); Pfizer Worldwide Research and Development, Cambridge, Massachusetts (N.C.P., R.S.P.S., A.S.K.); and Pfizer Worldwide Research and Development, La Jolla, California (B.B.)

ABSTRACT

The severe acute respiratory syndrome coronavirus 2 (SARS-CoV-2) 3C-like protease inhibitor PF-07321332 (nirmatrelvir), in combination with ritonavir (Paxlovid), was recently granted emergency use authorization by multiple regulatory agencies for the treatment of coronavirus disease 2019 (COVID-19) in adults and pediatric patients. Disposition studies on nirmatrelvir in animals and in human reagents, which were used to support clinical studies, are described herein. Plasma clearance was moderate in rats (27.2 ml/min per kg) and monkeys (17.1 ml/min per kg), resulting in half-lives of 5.1 and 0.8 hours, respectively. The corresponding oral bioavailability was moderate in rats (34%–50%) and low in monkeys (8.5%), primarily due to oxidative metabolism along the gastrointestinal tract in this species. Nirmatrelvir demonstrated moderate plasma protein binding in rats, monkeys, and humans with mean unbound fractions ranging from 0.310 to 0.478. The metabolism of nirmatrelvir was qualitatively similar in liver microsomes and hepatocytes from rats, monkeys, and humans; prominent metabolites arose via cytochrome P450 (CYP450)-mediated oxidations on the P1 pyrrolidinone ring, P2 6,6-dimethyl-3-azabicyclo[3.1.0]hexane, and the tertiary-butyl group at the P3 position. Reaction phenotyping studies in human liver microsomes revealed that CYP3A4 was primarily responsible (fraction metabolized = 0.99) for the oxidative metabolism of nirmatrelvir. Minor clearance mechanisms involving renal and biliary excretion of unchanged nirmatrelvir were also noted in animals and in sandwich-cultured human hepatocytes. Nirmatrelvir was a reversible and time-dependent inhibitor as well as inducer of CYP3A activity in vitro. First-in-human pharmacokinetic studies have demonstrated a considerable boost in the oral systemic exposure of nirmatrelvir upon coadministration with the CYP3A4 inhibitor ritonavir, consistent with the predominant role of CYP3A4 in nirmatrelvir metabolism.

SIGNIFICANCE STATEMENT

The manuscript describes the preclinical disposition, metabolism, and drug-drug interaction potential of PF-07321332 (nirmatrelvir), an orally active peptidomimetic-based inhibitor of the severe acute respiratory syndrome coronavirus 2 (SARS-CoV-2) 3CL protease, which has been granted emergency use authorization by multiple regulatory agencies around the globe for the treatment of coronavirus disease 2019 (COVID-19) in COVID-19-positive adults and pediatric patients who are at high risk for progression to severe COVID-19, including hospitalization or death.

Introduction

Coronaviruses are an assorted family of RNA viruses that can lead to respiratory, enteric, and neurologic diseases in humans and animals (Hu et al., 2021). Emerging coronaviruses of human health concern include two highly infectious coronaviruses, severe acute respiratory syndrome coronavirus (SARS-CoV) and Middle East respiratory syndrome

ABBREVIATIONS: AUC, area under the plasma concentration-time curve; BCRP, breast cancer resistance protein; CID, collision-induced dissociation; $CL_{biliary}$, biliary clearance; $CL_{biliary,int,app}$, apparent intrinsic biliary clearance; CL_{hep}, in vitro hepatic clearance; $CL_{int,app}$, apparent intrinsic clearance; CL_{plasma}, plasma clearance; $3CL^{pro}$, 3C-like protease; CL_{renal}, renal clearance; COVID-19, coronavirus disease 2019; CYP450, cytochrome P450; dNHBE, differentiated normal human bronchial epithelial; EC_{90}, 90% effective concentration; $F_a \times F_g$, fraction of the oral dose absorbed; f_{CL}, fractional clearance; f_m, fraction metabolized; HBD, hydrogen bond donor; HBSS, Hanks' balanced salt solution; HCD, high-energy C-trap dissociation; HEK, human embryonic kidney cells; HIF, human intestinal fluid; HLM, human liver microsome; HPLC, high-performance liquid chromatography; HSQC, multiplicity-edited heteronuclear single-quantum coherence; *J*, coupling constant; k_{inact}, maximal rate of inactivation; K_M, substrate concentration at half-maximal velocity; LC-MS/MS, liquid chromatography-tandem mass spectrometry; M1–M4, metabolites 1–4; MATE, multidrug and toxin extrusion protein; MDCK, Madin-Darby canine kidney; MDR1, multidrug resistance gene 1; MI, metabolic-intermediate; MTBE, methyl-tert-butyl ether; *m/z*, mass-to-charge ratio; m/z^+, protonated molecular ion; OAT, organic anion transporter; OATP, organic anion transporting polypeptide; OCT, organic cation transporter; oral F, oral bioavailability; P_{app}, apparent absorptive permeability; PF-00835231, N-((1S)-1-{[((1S)-3-hydroxy-2-oxo-1-{[(3S)-2-oxopyrrolidin-3-yl]-methyl}propyl)amino]carbonyl}-3-methylbutyl)-4-methoxy-1H-indole-2-carboxamide; PF-07321332, (nirmatrelvir, 1R, 2S, 5S)-N-{(1S)-1-Cyano-2-[(3S)-2-oxopyrrolidin-3-yl]ethyl}-6, 6-dimethyl-3-[3-methyl-N-(trifluoroacetyl)-L- valyl]-3-azabicyclo[3.1.0]hexane-2-carboxamide; PK, pharmacokinetics; SARS-CoV, severe acute respiratory syndrome coronavirus; SCHH, sandwich-cultured human hepatocyte; SGF, simulated gastric fluid; SIF, simulated intestinal fluid; $t_{1/2}$, half-life; TDI, time-dependent inhibition; T_{max}, time to reach C_{max}.

coronavirus (MERS-CoV), which were detected in humans in 2002 and 2012, respectively (Cui et al., 2019). A novel coronavirus termed as SARS-CoV-2 recently appeared in Wuhan, China, and led to an outbreak of uncommon viral pneumonia (Zhu et al., 2020). With high transmission rates, this new disease known as coronavirus disease 2019 (COVID-19) has quickly spread globally, resulting in 366 million confirmed COVID-19 cases and over 5.64 million deaths as of January 2022, according to Worldometer's Coronavirus Death Toll and Trends (https://www.worldometers.info/coronavirus/coronavirus-death-toll/). Isolation of the virus bronchoalveolar fluid from infected patients and genomic RNA sequencing indicated that the causative agent is a betacoronavirus that was not previously encountered. Despite the novelty, the genomic sequence identity of SARS-CoV-2 is similar to the one coded for SARS-CoV (∼79%) and MERS-CoV (∼50%) (Lu et al., 2020).

The SARS-CoV-2 genome contains two open reading frames that encode two large polyproteins (Ziebuhr et al., 1997; Zhou et al., 2020) from which functional proteins are generated through proteolysis. SARS-CoV-2 is known to encode a papain-like cysteine protease and a chymotrypsin-like cysteine protease known as main protease or 3C-like protease (3CL^{pro}) (Pillaiyar et al., 2016; Jin et al., 2020). The coronavirus 3CL^{pro} is a three-domain protease containing a Cys145-His41 catalytic dyad between domains I and II (Anand et al., 2003; Yang et al., 2003). A common structural feature among 3CL^{pro} substrates is the presence of a P1 Gln residue at the cleavage site, which is not encountered in any known human equivalent cysteine protease. This observation presents a unique opportunity in designing small-molecule inhibitors of 3CL^{pro} with relatively high selectivity over the human proteome (Rut et al., 2021).

During the 2002 SARS outbreak, we initiated efforts to identify small-molecule inhibitors of the SARS-CoV-1 3CL^{pro}, which led to the design of N-((1S)-1-{[((1S)-3-hydroxy-2-oxo-1-{[(3S)-2-oxopyrrolidin-3-yl]-methyl}propyl)amino]carbonyl}-3-methylbutyl)-4-methoxy-1H-indole-2-carboxamide (PF-00835231, Fig. 1) as a potent inhibitor of SARS-CoV-1 and more recently SARS-CoV-2 (Hoffman et al., 2020; Boras et al., 2021). The phosphate derivative (PF-07304814) of PF-00835231 is currently being studied as an intravenous (i.v.) treatment option in hospitalized COVID-19 patients (Boras et al., 2021). In response to the COVID-19 pandemic, we revitalized discovery efforts to identify orally active SARS-CoV-2 3CL^{pro} inhibitors using PF-00835231 as a starting point. A key objective in this exercise was to improve upon the poor oral absorption characteristics of PF-00835231 while retaining the favorable inhibitory effects against SARS-CoV-2 in recombinant enzyme and cellular antiviral assays. This research activity culminated in the design of (1R,2S,5S)-N-{(1S)-1-cyano-2-[(3S)-2-oxopyrrolidin-3-yl]ethyl}-6,6-dimethyl-3-[3-methyl-N-(trifluoroacetyl)-L-valyl]-3-aza-bicyclo[3.1.0]hexane-2-carboxamide (PF-07321332, nirmatrelvir) as an orally active antiviral agent (Owen et al., 2021). Nirmatrelvir inhibited [inhibition constant (K$_i$) = 3.11 nM] recombinant SARS-CoV-2 3CL^{pro} protease activity via a reversible covalent mechanism involving reaction of the cyano group with the catalytic Cys145 residue (see Fig. 1). Nirmatrelvir also repressed SARS-CoV-2 replication in physiologically relevant cellular systems such as differentiated normal human bronchial epithelial (dNHBE) cells and human adenocarcinoma-derived alveolar basal epithelial cells with unbound EC$_{90}$ (90% effective concentration) values of 181 nM and 215 nM, respectively. Oral administration of nirmatrelvir to a mouse-adapted SARS-CoV-2 model resulted in reduction of lung viral titers in a dose-dependent fashion and protected infected mice from lung tissue damage and weight loss (Owen et al., 2021). Preclinical disposition mechanisms of nirmatrelvir were characterized in animals and in human reagents to support animal safety and first-in-human clinical studies. The potential for pharmacokinetic (PK) interactions arising from inhibition/induction of major human cytochrome P450 (CYP450) enzymes and drug transporters was also examined in vitro systems. The collective results, including the demonstration of the predominant role for CYP3A4 in nirmatrelvir metabolism, which presented an option of boosting nirmatrelvir systemic exposure in humans by utilizing the CYP3A4 inhibitor ritonavir, are described herein.

Materials and Methods

Chemicals and Materials

Nirmatrelvir [chemical purity >99% by high-performance liquid chromatography (HPLC) and NMR] was synthesized at Pfizer Inc. (Groton, CT). Stock solutions of nirmatrelvir were prepared in either 100% dimethyl sulfoxide (DMSO)
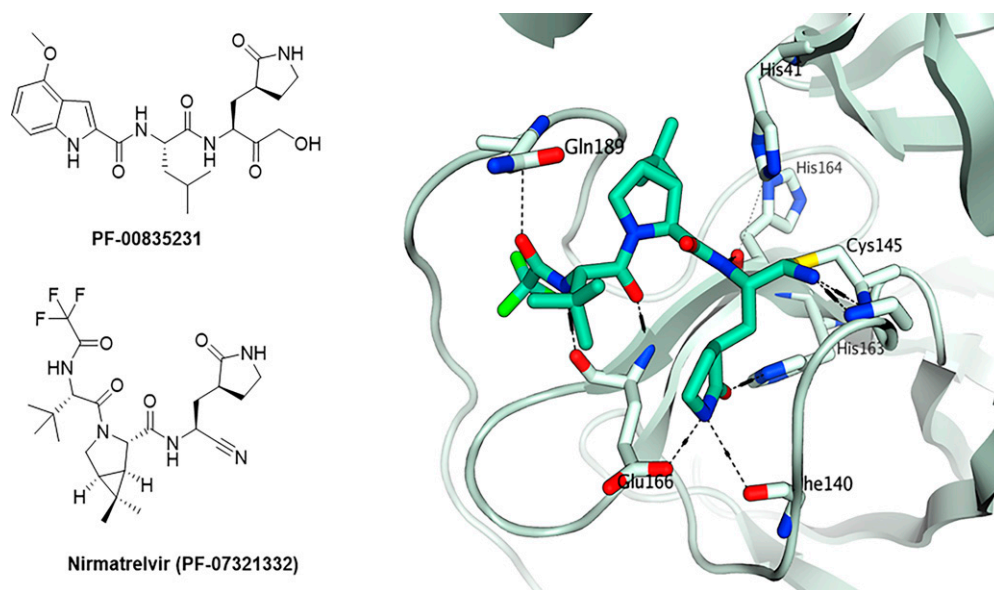
Fig. 1. Chemical structures of PF-00835231 (intravenous COVID-19 clinical candidate) and PF-07321332 (nirmatrelvir, oral COVID-19 clinical candidate) and binding mode of PF-07321332 in the 3CL^{pro} active site of SARS-CoV-2. PF-07321332 inhibits 3CL^{pro} activity via a reversible covalent bond formation between its nitrile group and an active site Cys145 residue.

or acetonitrile. Commercially obtained chemicals and solvents were of HPLC or analytical grade. In vitro studies were conducted on human tissue, which was acquired from a third party, and was confirmed as compliant with Pfizer policies, including Institutional Review Board/Independent Ethics Committee approval. Animal PK studies were conducted in agreement with federal, state, local, and institutional guidelines on the use of laboratory animals in research in AAALAC (Association for Assessment and Accreditation of Laboratory Animal Care)-accredited facilities and were approved by Pfizer's or Bioduro's (Shanghai, China) Institutional Animal Care and Use Committee. Description of experimental procedures for passive permeability, efflux, plasma protein/human liver microsomal binding, blood cell partitioning, liver microsome/hepatocyte stability, preclinical PK, CYP450 inhibition/induction and transporter inhibition, and liquid chromatography-tandem mass spectrometry (LC-MS/MS) assays for nirmatrelvir quantitation are provided as supplemental information.

Aqueous Solubility and Dissolution Measurement

Equilibrium solubility of crystalline nirmatrelvir in water was measured using an anhydrous form ('form 1') as well as a methyl-tert-butyl ether (MTBE) cosolvate form in duplicate, utilizing a temperature cycling method (Murdande et al., 2011). Briefly, nirmatrelvir was weighed in a screw-top vial, and an appropriate amount of water ($\geq$0.5 ml) was added. The vial was placed in an Environ-Genie incubator (Scientific Industries, Bohemia, NY) and a temperature cycling program (8 hours at 40°C, 5 hours at 15°C, followed by 12 hours at 25°C) was applied. After a pH measurement, the solutions were centrifuged (5 minutes, 14000 rpm) for particulate separation, and the supernatants assayed by ultrahigh-performance liquid chromatography for nirmatrelvir concentrations. Dissolution studies (Murdande et al., 2011) were performed with nirmatrelvir (150 mg, MTBE cosolvate or anhydrous 'form 1') in distilled water or 0.1 N HCl (500 ml) using a suspension of well dispersed nirmatrelvir particles in 0.5% w/v methyl cellulose. A dissolution test was conducted using a USP II dissolution apparatus (rotating at 100 rpm) with in-situ fiber optic UV-visible spectroscopy (Distek, Inc., North Brunswick, NJ).

Metabolic Stability in Intestinal Fluid

Fresh simulated gastric fluid (SGF) and simulated intestinal fluid (SIF) were prepared in house according to the US Pharmacopeia National Formulary (https://online.uspnf.com/uspnf/document/1_GUID-190BB90A-8350-41D4-82E0-88920705A993_1_en-US; https://online.uspnf.com/uspnf/document/1_GUID-4A435135-EDA6-4309-B967-0CE322595823_1_en-US). SGF was a solution of 3.2 g/l of pepsin and sodium chloride dissolved in deionized water (pH 1.2). SIF was a suspension of 10 g/l of pancreatin in monobasic potassium phosphate dissolved in deionized water (pH 6.8). Human intestinal fluid (HIF) (National BioService LLC, Saint Petersburg, Russia) was a mixture of pancreatic juice and bile obtained directly from the duodenum of two fasted adult volunteers via a surgical probe. An aliquot of SGF, SIF, or HIF was prewarmed to 37°C for 5 minutes followed by the addition of 1 μM nirmatrelvir (0.5% organic in final incubation, 200 μl final incubation volume). Incubations were conducted in duplicate or triplicate. At various time points (0.25, 10, 20, 40, 60, 90, and 120 minutes), a 20 μl aliquot of the incubation mixture was removed and quenched with acetonitrile (100 μl) containing diclofenac (25 ng/ml) as internal standard. Samples were vortexed and centrifuged (5 minutes, 2300 × g), and the supernatant (50 μl) was diluted with 200 μl of water. Quantitation of nirmatrelvir in the samples was performed using LC-MS/MS.

Biliary Excretion in Sandwich-Cultured Human Hepatocytes

Plateable cryopreserved human hepatocytes lot Hu4165 (female, Caucasian, age 57) were purchased from Invitrogen (Waltham, MA). The sandwich-cultured human hepatocyte (SCHH) methodology and data analysis applied here were described previously (Bi et al., 2006; Kimoto et al., 2017). Briefly, hepatocytes were plated in collagen-coated 24-well plates on day 1 at a density of 0.375 × 10^6 cells/well and overlaid with ice-cold matrigel after 18–24 hours of incubation. On day 5, SCHHs were first rinsed twice with Hanks' balanced salt solution (HBSS) containing Ca^{2+}/Mg^{2+} (standard) or Ca^{2+}/Mg^{2+}-free HBSS and then preincubated for 10 minutes with standard or Ca^{2+}/Mg^{2+}-free HBSS at 37°C. After aspirating the preincubation buffer, uptake was initiated by adding prewarmed nirmatrelvir (0.5 μM) to 37°C and terminated at a designated time (10 and 20 minutes) by adding ice-cold standard HBSS. Hepatocytes were lysed

with methanol containing an internal standard for quantification of PF-07321332 by LC-MS/MS. The in vitro apparent intrinsic biliary clearance ($CL_{biliary,int,app}$) was scaled up to a whole liver after application of physiologic scalars of (120 × 10^6 cells/g liver) × (21 g liver per kg body weight) to estimate the human biliary clearance ($CL_{biliary}$) (Kimoto et al., 2017).

Metabolite Identification

Nirmatrelvir (10 μM) was incubated in Wistar-Han rat (male and female), cynomolgus monkey (male), and pooled (mixed sex of 50) human liver microsomes (HLMs) (protein concentration = 2 mg/ml) (Sekisui XenoTech, Kansas City, KS) or recombinant human CYP450 enzymes (CYP1A1, CYP1A2, CYP1B1, CYP2A6, CYP2B6, CYP2C8, CYP2C9, CYP2C18, CYP2C19, CYP2D6, CYP2E1, CYP2J2, CYP3A4, CYP3A5, CYP3A7, and CYP4F2; 100 pmol/ml each) (Corning, Glendale, AZ) in 100 mM potassium phosphate buffer (pH 7.4) containing β-nicotinamide adenine dinucleotide phosphate, reduced form (NADPH) (1.3 mM), $MgCl_2$ (3.3 mM) at 37°C for 1 hour. Incubations were quenched with acetonitrile (0.6 ml). Because nirmatrelvir possesses very poor UV absorbance, a second set of incubations were generated where the parent compound was only added after the acetonitrile quench. These incubations mixtures, used to assess metabolite formation by HPLC-UV, ensured an improved delineation of nirmatrelvir-related material from other components in the incubations. The quenched incubation mixtures were centrifuged (5 minutes, 1800 × g), and the supernatants were evaporated to dryness. Metabolite identification in hepatocytes was performed in nirmatrelvir (10 μM) incubations with Wistar-Han rat (male, pool of 24 animals), cynomolgus monkey (male, pool of three animals), and human (pool of 13 donors of mixed sex) hepatocytes (Bio-IVT, Baltimore, MD) at 0.75 × 10^6 cells/ml. Periodic aliquots were removed at 0, 1, and 4 hours and quenched with five volumes of acetonitrile. Samples were centrifuged (5 minutes, 1800 × g) and evaporated to dryness using a Genevac evaporative centrifuge.

LC-MS/MS Analysis for Metabolite Identification

The residues were reconstituted in 50–150 μl of 1% formic acid containing 20% acetonitrile and analyzed by ultrahigh-performance liquid chromatography-UV-high-resolution mass spectrometry operated in positive ion mode using an Orbitrap Elite mass spectrometer in line with a Vanquish HPLC-UV with cooled autoinjector (Thermo Fisher, Waltham, MA). Injection volumes were 5–15 μl, depending on the experimental run. A Kinetex XB C18 column (Phenomenex, Torrance, CA) was used (2.1 × 100 mm, 2.6 μm) with a flow rate of 0.4 ml/min heated to 45°C. Mobile phase A was comprised of 0.1% formic acid in water, and mobile phase B was comprised of acetonitrile. The mobile phase composition began at 5% B held for 0.5 minutes followed by a linear gradient to 70% B at 11 minutes, a second linear gradient to 95% B at 13 minutes, a 1-minute wash at 95% B, and finally a 2-minute re-equilibration period at 5% B. UV was monitored between 200 and 400 nm, and chromatograms were reconstructed using λ at 200 nm.

Biosynthesis of Nirmatrelvir Metabolites for Structural Elucidation

Nirmatrelvir (25 μM), HLMs (2 mg/ml), $MgCl_2$ (3.3 mM), and NADPH (1.3 mM) were incubated in potassium phosphate buffer (100 mM, pH 7.4) (40 ml) at 37°C for 55 minutes, followed by the addition of acetonitrile (40 ml). The solution was centrifuged (1800 × g) for 5 minutes and concentrated in a Genevac vacuum centrifuge. The remaining mixture was treated with acetonitrile (0.5 ml), formic acid (0.5 ml), and water to a volume of 50 ml. This mixture was centrifuged (30 minutes, 40000 × g), and the supernatant was injected into a Polaris C18 column (Agilent, Santa Clara, CA) (4.6 × 250 mm; 5 μm) through a Jasco HPLC pump (Jasco Inc., Easton, MD) at 0.8 ml/min. After injection, the column was moved to an Acquity HPLC-UV in line with a CTC Analytics fraction collector (Zwingen, Switzerland) and linear trap quadrupole Velos mass spectrometer (Thermo Fisher). The material was eluted with a mobile phase A (0.1% formic acid in water) and mobile phase B (acetonitrile) at a flow rate of 0.8 ml/min. The gradient was initiated at 2% mobile phase B with a linear gradient to 15% mobile phase B at 5 minutes, a second linear gradient to 60% mobile phase B at 85 minutes, and a third linear gradient to 95% mobile phase B at 90 minutes. This composition was held for 9 minutes, followed by a 10-minute re-equilibration period to initial conditions. The eluent was passed through the UV detector and then a splitter that directed the flow to the fraction collector and mass spectrometer in an approximate 15:1 ratio. Fractions were collected every

20 seconds, and those containing metabolites of interest were evaluated for purity by ultrahigh-pressure LC-MS with UV detection described above to facilitate pooling. Pooled fractions were evaporated in a vacuum centrifuge, and residues were evaluated by NMR spectroscopy for structural elucidation.

NMR Spectroscopy

Samples were dissolved in DMSO-d_6 "100%" (0.045 ml) (Cambridge Isotope Laboratories, Andover, MA) and placed in an NMR tube (1.7 mm) in a dry argon atmosphere. ^{1}H and ^{13}C spectra were referenced using residual DMSO-d_6 (^{1}H δ = 2.50 ppm relative to tetramethylsilane, δ = 0.00; ^{13}C δ = 39.50 ppm relative to tetramethylsilane, δ = 0.00). NMR spectra were recorded on a Bruker Avance 600 MHz (Bruker BioSpin Corporation, Billerica, MA) controlled by Topspin V4.0 and equipped with a 1.7 mm TCI Cryo probe. 1D spectra were recorded using an approximate sweep width of 8400 Hz and a total recycle time of approximately 7 seconds. The resulting time-averaged free induction decays were transformed using an exponential line broadening of 1.0 Hz to enhance signal to noise. For through-space experiments (rotating-frame Overhauser effect or nuclear Overhauser effect), the sample temperature was raised to 340 Kelvin. Two-dimensional NMR data were recorded using the standard pulse sequences provided by Bruker. At minimum, a 1K × 128 data matrix was acquired using a minimum of two scans and 16 dummy scans with a spectral width of 10,000 Hz in the f2 dimension. The 2D data sets were zero-filled to at least 1K data point. Post-acquisition data processing was performed with either Topspin V3.2 or MestReNova V9.1. A series of standard 1D and 2D NMR experiments were performed on each sample.

Enzyme Kinetics of Nirmatrelvir Metabolite Formation in HLMs

Experimental conditions used in the kinetics study design were chosen to yield linear reaction velocities as determined from preliminary range-finding experiments. To determine the rates of metabolite formation, nirmatrelvir (0.02–200 μM) was incubated with HLMs (pool of 50 mixed gender donors; Sekisui Xeno-Tech) diluted to 0.3 mg/ml microsomal protein in 100 mM potassium phosphate buffer (pH 7.4) supplemented with MgCl$_2$ (3.3 mM) and NAPDH (1.3 mM) for a final incubation volume of 300 μl. Nirmatrelvir stock solutions were prepared by serial dilution in acetonitrile such that the final concentration of acetonitrile in the incubations was 1.0%. Incubations were conducted at 37°C in duplicate. After 15 minutes, aliquots of the incubation mixture (200 μl) were quenched with acetonitrile (600 μl) containing internal standard (25 ng/ml diclofenac). Samples were vortexed and centrifuged (5 minutes, 2300 × g), and the supernatant was diluted with an equal volume of water. Samples were analyzed by LC-MS/MS for quantitation of nirmatrelvir oxidative metabolites M1 (PF-07329265), M2 (PF-07329266), M3 (PF-07329267), and M4 (PF-07329268), for which authentic standards were available through biochemical synthesis.

The LC-MS/MS system consisted of a Sciex Triple Quadrupole 5500 mass spectrometer (Sciex, Framingham, MA) equipped with an electrospray ion source and Agilent 1290 binary pump. Aqueous mobile phase (A) was composed of water with 0.1% formic acid, and organic mobile phase (B) consisted of acetonitrile with 0.1% formic acid. Samples (10 μl) from various in vitro incubations were injected onto a Kinetex XB-C18 (2.1 × 50 mm, 2.6 μm) (Phenomenex, Torrance, CA) column maintained at room temperature with a flow rate of 0.5 ml/min. The gradient program began with 10% mobile phase B held for 0.2 minutes, followed by a linear gradient to 40% B over 2.3 minutes, then to 98% over 0.3 minutes, held at 98% B for 0.6 minutes, followed by re-equilibration to initial conditions for 0.3 minutes. The mass spectrometer was operated in positive detection mode with the following analyte mass transitions (Q1/Q3): diclofenac 296/250, nirmatrelvir 500/110, PF-07329265 (M1) 516/126, PF-07329266 (M2) 516/289, PF-07329267 (M3) 516/291, and PF-07329268 (M4) 498/110 (optimized Q1 mass representing loss of H$_2$O in the source). The range of analyte concentration for standard curve was 0.25–250 nM (M1 and M4) and 0.25–100 nM (M2 and M3). Integration and quantitation of metabolite and internal standard peak areas were performed using Analyst version 1.7 (Sciex) to derive the analyte to internal standard peak area ratios. Standard curves for the quantitation of metabolite concentration were prepared from plots of concentration versus area ratio and analyzed using a linear regression with $1/x^2$ weighting.

Data Analysis

Formation rates (v) were calculated by dividing the measured metabolite concentration by incubation time and protein concentration of the incubation. The Michaelis-Menten model was used to derive the apparent enzyme kinetic parameters V$_{max}$ (maximal velocity) and K$_M$ (substrate concentration at half-maximal velocity) using GraphPad Prism version 8.02 (La Jolla, CA):

$$v = \left(\frac{V_{max} \times S}{K_M + S} \right) \quad (1)$$

Assessment of the enzyme kinetics was conducted by visual inspection of the Eadie-Hofstee diagrams constructed from the plot of v versus the ratio of v and substrate concentration (Nagar et al., 2014):

$$v = -K_M \left(\frac{v}{S} \right) + V_{max} \quad (2)$$

When observations of nonlinear kinetics in Eadie-Hofstee plots for metabolite formation data were suggestive of multienzyme contribution, fitting to a two-enzyme nonsaturable Michaelis-Menten model was attempted:

$$v = \left(\frac{V_{max1} \times S}{K_{M1} + S} \right) + \left(CL_{int(2)} \times S \right) \quad (3)$$

where subscript 1 represents a high-affinity/low-capacity enzyme and CL$_{int(2)}$ represents the apparent intrinsic clearance rate of the secondary low-affinity/high-capacity enzyme (Nagar et al., 2014).

Alternately, for metabolite formation profiles showing characteristics of allosteric sigmoidal in the Eadie-Hofstee plots, the following equation was used to fit the data:

$$v = \left(\frac{V_{max} \times S^h}{K_{half}^h + S^h} \right) \quad (4)$$

where K$_{half}$ is the enzyme concentration that gives a half-maximal velocity and h is the Hill slope. Assessment of best fit was based on a number of criteria, including visual inspection of the data plots (Michaelis-Menten and Eadie-Hofstee), distribution of the residuals, size of the sum of the squared residuals, and the standard error of the estimates. Selection of a model other than Michaelis-Menten was based on the F-test ($P < 0.05$) or the Akaike Information Criterion (Nagar et al., 2014). In vitro apparent intrinsic clearance (CL$_{int,app}$) and scaled apparent intrinsic clearance (CL$_{int,app,sc}$) were calculated for each metabolic pathway using the following equations:

$$CL_{int,\,app} = \frac{V_{max}}{K_M} \quad (5)$$

$$CL_{int,\,app,\,sc} = CL_{int,\,app} \times \frac{45 \text{ mg protein}}{\text{g liver}} \times \frac{21 \text{ g liver}}{\text{kg body weight}} \quad (6)$$

Unbound CL$_{int}$ values were calculated by dividing the respective CL$_{int}$ by the unbound liver microsomal free fraction (f$_{u,mic}$) determined in HLMs using equilibrium dialysis. When necessary, the measured f$_{u,mic}$ was scaled to reflect the respective microsomal protein concentration according to the method of Austin et al. (2002). The fractional contribution by an individual metabolic pathway (f$_{CL(HLM)}$) in HLMs to the total in vitro clearance of PF-07321332 was calculated as:

$$f_{CL(HLM)} = \frac{CL_{int,\,app,\,x}}{CL_{int,\,app,\,all}} \quad (7)$$

where CL$_{int,app,x}$ is the intrinsic clearance for metabolite x and CL$_{int,app,all}$ is the sum of in vitro CL$_{int}$ values for all metabolites monitored.

Multipoint Selective Inhibition of CYP3A4/5 Activity in HLMs

The effect of CYP3A-selective inhibition by ketoconazole on nirmatrelvir oxidative metabolite formation was assessed in HLMs. Incubations (0.3 ml) were conducted in 100 mM potassium phosphate buffer (pH 7.4) containing MgCl$_2$ (3.3 mM), NADPH (1.2 mM), HLMs (0.3 mg/ml), and nirmatrelvir (2.5 μM) at 37°C for 15 minutes in the absence or presence of varying concentrations of ketoconazole (0.001–10 μM). Chemical inhibition experiments were conducted in triplicate. Sample bioanalysis for analyte quantitation was performed using LC-MS/MS as previously described in the enzyme kinetics protocol.

The maximum contribution of CYP3A to nirmatrelvir metabolism in HLMs was determined by the percent activity remaining of each metabolite in the presence of a broad concentration range of ketoconazole (0.001–10 μM). The percent activity remaining was obtained by normalizing concentration data to the averaged solvent controls. Curve fitting of the activity versus inhibitor concentration data by nonlinear regression to a four-parameter inhibition model was conducted

using GraphPad Prism:

$$Y = Bottom + \frac{Top - Bottom}{1 + \left(\frac{10^{LogIC_{50}}}{10^X}\right)^{HillSlope}} \quad (8)$$

where bottom is the minimum activity, top is the maximal activity, IC_{50} is the inhibitor concentration at half maximal activity, X is the inhibitor concentration, and Y is percent of enzyme activity remaining. The maximal contribution by the CYP450 isoform was determined as the difference between the maximum and minimum percent activity remaining based on data fitting.

The fraction of nirmatrelvir metabolized (f_m) to a single metabolite x by a specific CYP450 isoform z ($f_{mMx,CYPz}$) was calculated using the following equation:

$$f_{mMx,CYPz} = f_{INH} \times f_{CL} \quad (9)$$

where f_{INH} is the scaled fraction of metabolite (M) x inhibited by a CYP450 specific inhibitor z and f_{CL} is the fraction of nirmatrelvir clearance represented by metabolite x determined from enzyme kinetic experiments.

Single-Point Selective Inhibition of CYP3A4 versus CYP3A5 Activity in HLMs

Nirmatrelvir (2.5 μM) was incubated with HLMs pooled from CYP3A5*1/*1 (extensive metabolizers) (Sekisui XenoTech) in the presence of selective chemical inhibitors ketoconazole (1 μM) (CYP3A4/5) and CYP3cide (1 μM) (CYP3A4) for the determination of CYP3A4 and CYP3A5 isoform contribution to the metabolism of nirmatrelvir. Incubations (0.3 ml) were conducted in 100 mM potassium phosphate buffer (pH 7.4) containing MgCl$_2$ (3.3 mM), NADPH (1.2 mM), and 0.3 mg/ml HLMs at 37°C for 15 minutes in a heat block. Chemical inhibition studies were conducted in triplicate. Stock solutions of ketoconazole and CYP3cide were prepared in 50/50 methanol/H$_2$O. The microsome mixtures containing inhibitor and NADPH were warmed for 5 minutes (keto) or 10 minutes (CYP3cide) prior to initiating the reaction by addition of nirmatrelvir. Solvent control incubations were performed in the absence of chemical inhibitors. Sample bioanalysis for analyte quantitation was performed using LC-MS/ MS as previously described in the enzyme kinetics procedure. To discern the contributions of CYP3A4 and CYP3A5 isoforms to nirmatrelvir metabolism in HLMs, the differential effects of CYP3A and CYP3A4 selective chemical inhibitors on metabolite formation rate were calculated using the following formula:

$$\%Inhibition \ (unscaled) = \left(1 - \frac{v_{inh}}{v_{ctrl}}\right) \times 100\% \quad (10)$$

where v_{inh} is the formation rate in the presence of inhibitor and v_{ctrl} is the formation rate in the solvent control incubation. Determination of CYP3A5 contribution to each metabolic pathway was calculated as the difference in percent inhibition by ketoconazole (CYP3A4/5) versus CYP3cide (CYP3A4) in HLM 3A5 *1/*1. Statistical analyses were conducted using GraphPad v. 8.02 to determine the statistical significance of inhibitor effect on metabolite formation rate versus minus inhibitor solvent control and between the effects of ketoconazole versus CYP3cide, using a one-way ANOVA analysis with a Bonferonni's Test for multiple comparisons. Statistical significance was set at $\alpha = 0.01$.

Results

Passive Permeability, Efflux Potential, and Solubility Characteristics of Nirmatrelvir

Nirmatrelvir (molecular weight = 499.53) is a moderately lipophilic (LogP = 1.68) neutral compound, which demonstrated low apparent passive permeability (P_{app}) of 1.76×10^{-6} cm/s in the low-efflux Madin-Darby canine kidney (MDCKII-LE) cell assay (Di et al., 2011). In Caco-2 cell monolayers, nirmatrelvir (0.11–231 μM) also exhibited low apical (A) to basolateral (B) permeability, with values ranging from 0.66 to 1.19×10^{-6} cm/s (Supplemental Table 1). Coincubation of nirmatrelvir (0.32 μM) with an efflux inhibitor cocktail comprised of 10 μM Ko143 [breast cancer resistance protein (BCRP) inhibitor], 10 μM PSC833 [multidrug resistance gene 1 (MDR1) inhibitor], and 100 μM MK571 (multidrug resistance protein inhibitor) led to a considerable increase in the apparent permeability of nirmatrelvir from 0.80 ± 0.15 to 4.05 ± 0.26 cm/s (see Supplemental Table 1).

The substrate properties of nirmatrelvir toward human MDR1 and BCRP efflux transporters were examined in transporter-transfected MDCK cells by measuring the bidirectional permeability (P_{app} AB and P_{app} BA) (Supplemental Table 2). In MDCKI-MDR1 cells, nirmatrelvir (0.3–3.0 μM) demonstrated mean P_{app} (AB) and P_{app} (BA) values ranging from 0.12 to 0.21 ($\times 10^{-6}$ cm/s) and 9.94 to 10.3 ($\times 10^{-6}$ cm/s), respectively, resulting in efflux ratios of 48.4–83.7 across the concentration range. Inclusion of the MDR1 inhibitor PSC833 (5 μM) in the incubation mixtures led to a dramatic reduction (48–84 → 1.7–2.3) in nirmatrelvir efflux ratios. Under these experimental conditions, the prototypic MDR1 substrate quinidine (0.5 μM) demonstrated mean P_{app} (AB), P_{app} (BA), and efflux ratio values of 1.4 ($\times 10^{-6}$ cm/s), 78 ($\times 10^{-6}$ cm/s), and 58, respectively. Inclusion of the MDR1 inhibitor PSC833 (5 μM) decreased the efflux ratio of quinidine from ~58 to 1.0. The efflux ratio of nirmatrelvir (0.3–3.0 μM) in MDCKII-BCRP cells ranged from 1.4 to 1.5, suggesting that nirmatrelvir was not a substrate of human BCRP. Under these experimental conditions, the known BCRP substrate pitavastatin demonstrated mean P_{app} (AB) and P_{app} (BA) values of 0.4 ($\times 10^{-6}$ cm/s) and 11 ($\times 10^{-6}$ cm/s), respectively, which resulted in an efflux ratio of ~25. Inclusion of the selective BCRP inhibitor Ko143 (5 μM) led to a significant decrease of the pitavastatin efflux ratio from 25 to 0.2.

The equilibrium solubility of crystalline nirmatrelvir-MTBE cosolvate and anhydrous 'form 1' in unbuffered water was 7.21 mg/ml (pH 7.9) and 1.2 mg/ml (pH 7.0), respectively. The dissolution of crystalline nirmatrelvir-MTBE cosolvate in water was ~20 times faster than crystalline nirmatrelvir anhydrous 'form 1.' The likelihood of a peptidase-mediated hydrolytic cleavage across the peptide backbone in nirmatrelvir was examined in gastrointestinal fluids, which included SIF and SGF and intestinal fluid from healthy human volunteers (Smart et al., 2014; Wang et al., 2015). Nirmatrelvir (1 μM) was stable [half-life ($t_{1/2}$) > 240 minutes] toward hydrolytic cleavage in 2-hour incubations with SIF, SGF, and HIF.

Plasma Protein Binding, Blood-to-Plasma Partitioning, and Nonspecific HLM Binding of Nirmatrelvir

Nirmatrelvir (0.3–10 μM) demonstrated moderate and concentration-independent plasma protein binding in rats, monkeys, and humans with mean unbound plasma fractions ($f_{u,p}$) of 0.478, 0.434, and 0.310, respectively (Supplemental Table 3). Nirmatrelvir (0.3–10 μM) was stable in rat, monkey, and human plasma for ~6 hours at 37°C. The mean (± S.D.) blood-to-plasma ratios (BPRs) for nirmatrelvir (1 μM) in rats, monkeys, and humans were 0.83 ± 0.049, 0.68 ± 0.024, and 0.60 ± 0.024, respectively, suggesting that nirmatrelvir distributed into plasma preferentially over red blood cells. The mean (± S.D.) of unbound fraction of nirmatrelvir (2 μM) in HLMs (1 mg/ml protein concentration) was 0.824 ± 0.017.

Metabolic Stability Studies with Nirmatrelvir

The metabolic stability of nirmatrelvir (1 μM) was examined in liver microsomes (fortified with NADPH) and cryopreserved hepatocytes from rats, monkeys, and humans using a substrate depletion assay format (Table 1). Nirmatrelvir did not demonstrate metabolic turnover in liver microsomes from animals and humans when NADPH was excluded from the incubations. In the presence of NADPH, nirmatrelvir demonstrated low metabolic turnover ($CL_{int,app}$ = 6.1 μl/min per mg) in rat liver microsomes but underwent extensive metabolism ($CL_{int,app}$ = 161 μl/min per mg) in liver microsomes from monkeys. Metabolic turnover in NADPH-supplemented HLMs was moderate ($CL_{int,app}$ = 28.8 μl/min per mg, unbound $CL_{int,app}$ = 34.9 μl/min per mg). In cryopreserved hepatocytes from rats, monkeys, and humans, nirmatrelvir demonstrated low total $CL_{int,app}$ (μl/min per 10^6 cells) of 4.64, 10.3, and

TABLE 1

Metabolic stability of nirmatrelvir in liver microsomes and hepatocytes

Reagent	Cofactor	$t_{1/2}$ (min)[a]	$CL_{int,app}$ (μl/min per mg or μl/min per 10^6 cells)	CL_{hep} (ml/min per kg)	Observed CL_{plasma} (ml/min per kg)[b]
Liver Microsomes[c]					
Rat	NADPH	114	6.08	5.8	22.7
Monkey	NADPH	4.31	161	25	15.8
Human	NADPH	24.1	28.8	6.3	—
Hepatocytes[d]					
Rat	NA	300	4.64	11	22.7
Monkey	NA	135	10.3	13	15.8
Human	NA	280	5.16	3.2	—

NA, not applicable.
[a]Stability data governed by $t_{1/2}$ was scaled to $CL_{int,app}$ and CL_{hep} using the well stirred model (see supplemental material).
[b]Depicted in vivo CL_{plasma} is after subtracting CL_{renal} in the respective species.
[c]Metabolic stability of nirmatrelvir (0.1 or 1.0 μM) was examined in NADPH-supplemented liver microsomes from rats, monkeys, and humans (1 mg/ml protein concentration) for 60–80 min at 37°C. Liver microsomal stability studies were conducted in triplicate.
[d]Metabolic stability of nirmatrelvir (1.0 μM) was examined in hepatocytes from rats, monkeys, and humans (0.5 × 10^6 cells/ml) for 240 min at 37°C. Hepatocyte stability studies were done in duplicate.

5.16, respectively. The total $CL_{int,app}$ in liver microsomes and hepatocytes wase scaled to yield the corresponding hepatic clearance (CL_{hep}) values (Table 1) using the well stirred model (Di et al., 2012).

Metabolite Characterization

Figures 2 and 3 depict HPLC-UV chromatogram of incubation mixtures of nirmatrelvir (10 μM) in NADPH-supplemented liver microsomes and cryopreserved hepatocytes from rats, monkeys, and humans, respectively. Elucidated structures of the metabolites based on mass and ^{1}H NMR spectral data are depicted in Fig. 4. A total of five oxidative metabolites were observed in liver microsomes to varying degrees across rats, monkeys, and humans. The metabolites were derived from monohydroxylation (metabolites M1–M4) and dehydrogenation [mass-to-charge ratio (m/z) 498]. Although metabolism in hepatocytes was apparently slower than in liver microsomes under the conditions examined, a similar metabolic profile was observed in the two matrices.

There were no human-unique metabolites of nirmatrelvir; all metabolites observed in HLMs and human hepatocytes were also characterized in liver microsomes and hepatocytes from rats and monkeys. The regiochemistry of oxidation was tentatively assigned based on comparison of the mass spectral fragmentation data for the parent and its oxidized products. Structures of metabolites M1–M4 were unambiguously identified via NMR characterization of the biosynthesized samples obtained from scaled-up incubations of nirmatrelvir in NADPH-fortified HLMs.

Nirmatrelvir

A protonated molecular ion (m/z^+) of 500.2473 was observed for nirmatrelvir, which is consistent with a molecular formula of $C_{23}H_{33}N_5O_4F_3$ (−1.23 ppm). Diagnostic fragment ions in the collision-induced dissociation (CID) spectrum included m/z 319.1625 (cleavage of the acyl moiety on the 2-position of the [3.1.0]azabicyclic ring) and m/z 291.1813 (cleavage of the acyl moiety on the 3-position of the
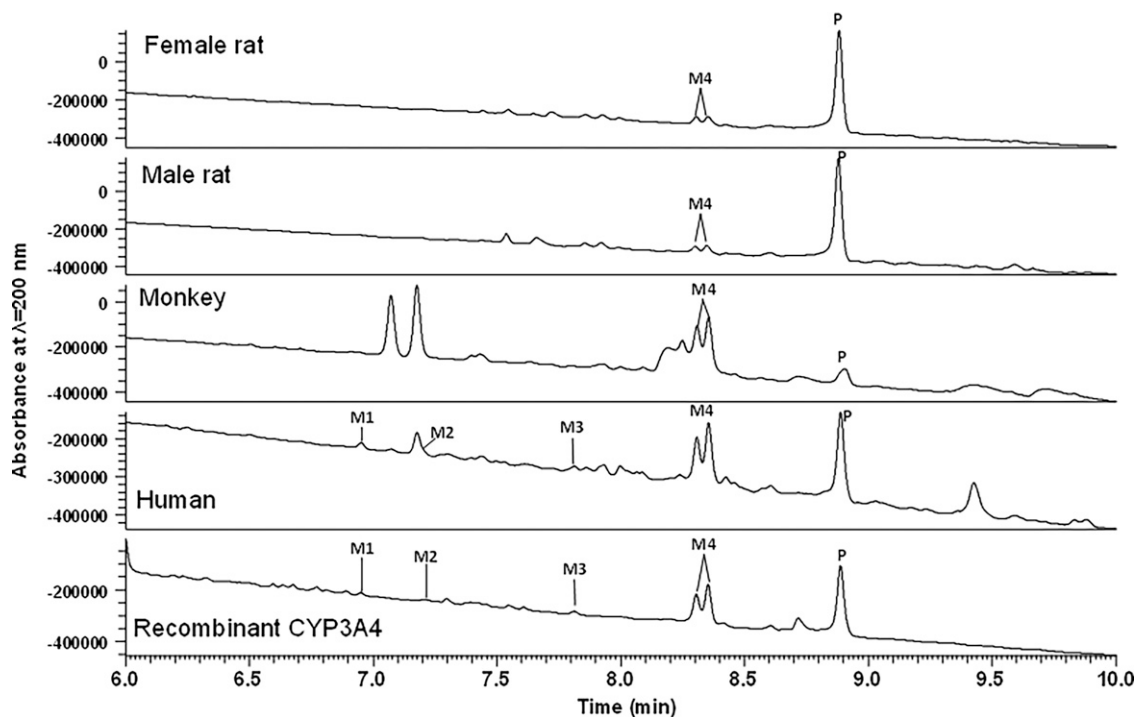

Fig. 2. HPLC-UV chromatograms of NADPH-supplemented liver microsomal incubations and human recombinant CYP3A4 with PF-07321332 (nirmatrelvir, 10 μM). Drug-related peaks are denoted with P for parent drug and M for metabolites. All unmarked peaks represent nondrug-related interferences present in control incubations (not shown). Metabolite M2 in the human liver microsomal incubation is a shoulder on the larger interfering peak. Metabolite M4 is present as two closely eluting peaks representing the two interconverting diastereomers.
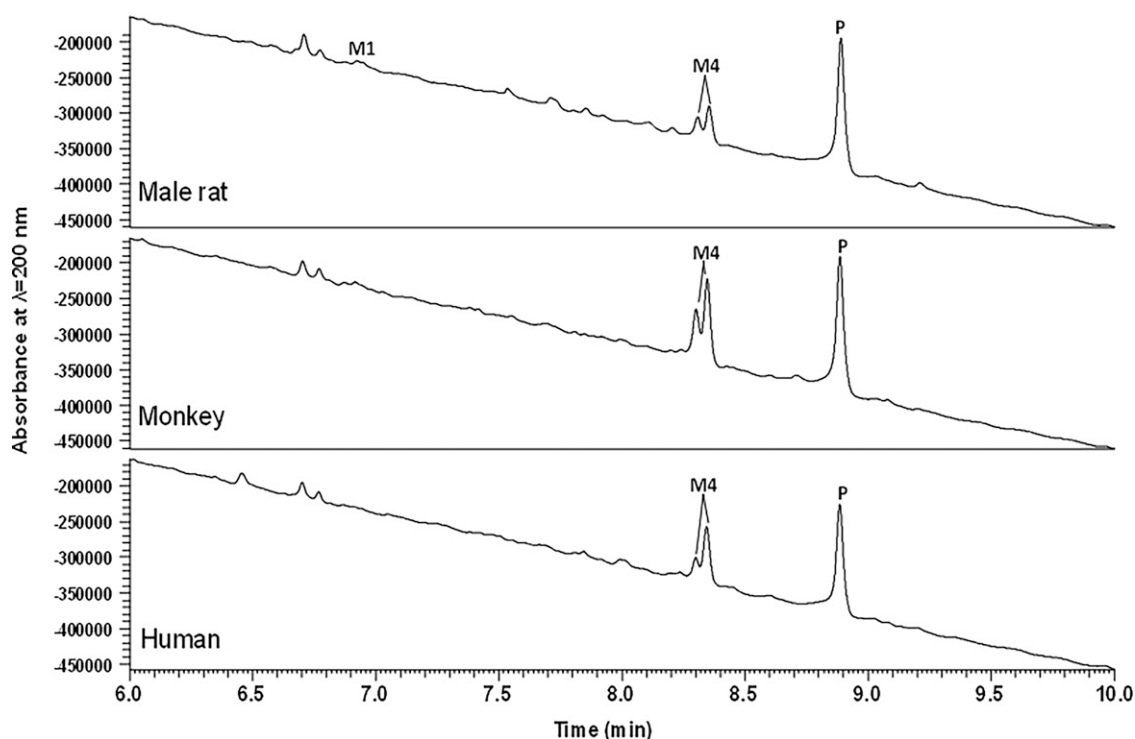
Fig. 3. HPLC-UV chromatograms of cryopreserved primary hepatocyte incubation extracts for nirmatrelvir (10 μM). Drug-related peaks are denoted with P for parent drug and M for metabolites. All unmarked peaks represent nondrug-related interferences present in control incubations (not shown). Metabolite M4 is present as two closely eluting peaks representing the two interconverting diastereomers.

[3.1.0]azabicyclic ring), which yielded opposing portions of nirmatrelvir. Further fragmentation of m/z 319 yielded the [3.1.0]azabicyclic ring (m/z 110.0964) such that modifications of this portion of the molecule were readily observable in the mass spectra (see elucidation of M1 and M2 below).

The ^{1}H NMR spectra of nirmatrelvir (Supplemental Fig. 1) contains three amide resonances assigned to three hydrogens—H14: δ 9.41 [d, coupling constant (J) = 8.1 Hz, 1H]; H17: 9.02 (d, J = 8.4 Hz, 1H); and H23: 7.67 (s, 1H). Additionally, the ^{1}H NMR spectra of
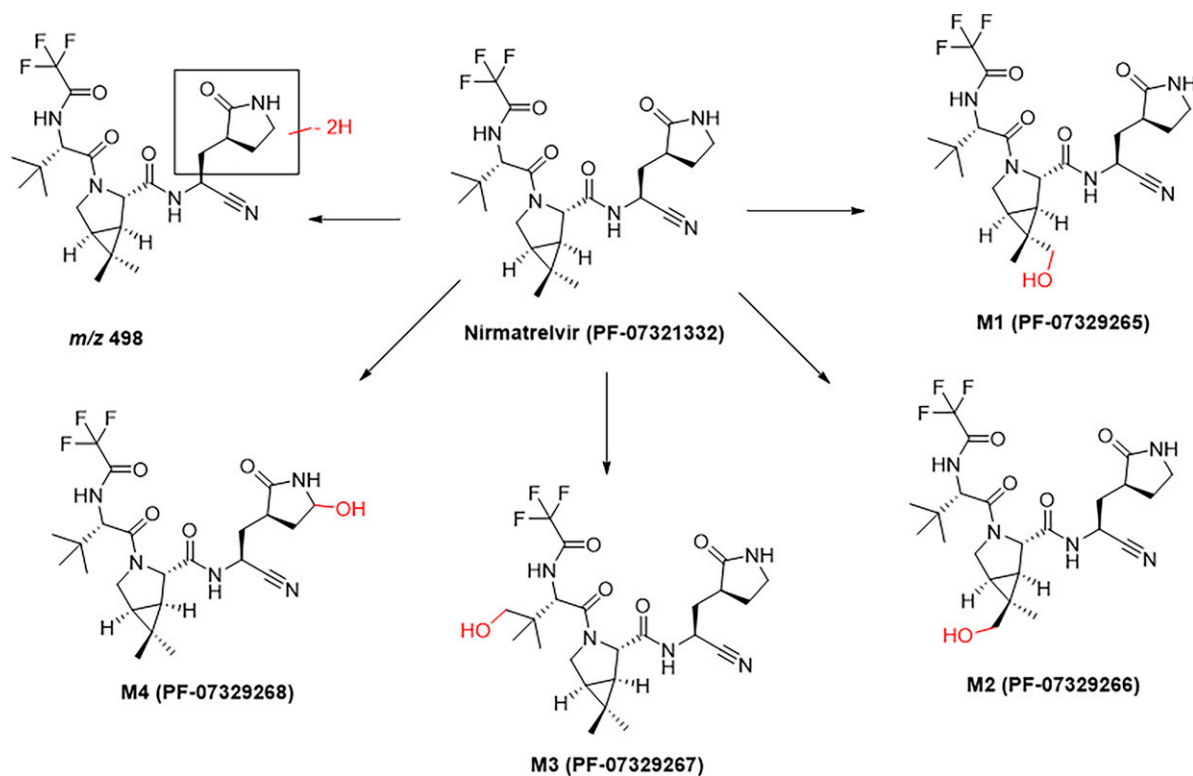

Fig. 4. Metabolites of PF-07321332 (nirmatrelvir) in liver microsomes and hepatocytes from rats, monkeys, and humans.

nirmatrelvir contains 15 aliphatic resonances assigned to 29 hydrogens—H18: 4.98 (m, 1H); H13: 4.42 (d, $J = 8.3$ Hz, 1H); H6: 4.17 (s, 1H); H2": 3.92 (dd, $J = 10.0, 5.4$ Hz, 1H); H2': 3.70 (d, $J = 10.4$ Hz, 1H); H22': 3.15 (t, $J = 8.9$ Hz, 1H); H22": 3.05 (q, $J = 8.9$ Hz, 1H); H20: 2.41 (m, 1H); H19"/21": 2.12 (m, 2H); H19'/21': 1.72 (m, 2H); H3: 1.58 (t, $J = 6.3$ Hz, 1H); H5: 1.33 (d, $J = 7.5$ Hz, 1H); H9: 1.04 (s, 3H); H26/32/33: 0.99 (s, 9H); and H10: 0.86 (s, 3H).

Metabolite M1 (PF-07329265)

Metabolite M1 (designated as PF-07329265) possessed a protonated molecular ion of m/z^+ 516.2435, consistent with a molecular formula of $C_{23}H_{33}N_5O_5F_3$ (1.3 ppm), which was indicative of a monohydroxylation in nirmatrelvir. The dominant fragment ion (m/z 335.1585) in the CID spectrum of PF-07329265 suggested that the N-((S)-1-cyano-2-((S)-2-oxopyrrolidin 3-yl)ethyl)formyl portion in nirmatrelvir was not modified (Supplemental Fig. 2). In the high-energy C-trap dissociation (HCD) spectrum, the fragment ion of m/z 126.0917 is diagnostic of the region of hydroxylation being the 6,6-dimethyl-3-azabicyclo[3.1.0]hexane fused ring.

The ^{1}H NMR spectrum (Supplemental Fig. 3) of biosynthesized PF-07329265 revealed that only the resonances of the methyl hydrogens (H9 and H10) of the 6,6-dimethyl-3-azabicyclo[3.1.0]hexane fused ring had changed significantly from those observed in the ^{1}H NMR spectrum of nirmatrelvir. Notably, the ^{1}H methyl resonance observed at δ 1.04 in nirmatrelvir was absent in isolated PF-07329265, and a new resonance was observed at δ 3.24, which integrated to two hydrogens. In the ^{1}H-^{13}C multiplicity-edited heteronuclear single-quantum coherence (HSQC) data of the isolate, this new resonance correlated to a carbon with a chemical shift of δ 67.9 (Supplemental Fig. 4, B and C). The integration and ^{1}H and ^{13}C chemical shifts of this new resonance are all consistent with the oxidation of one of the geminal-dimethyl groups on the azabicyclohexane moiety.

To determine the configuration of this stereocenter, a series of rotating-frame Overhauser effect experiments was performed (Supplemental Fig. 4, D–F). Irradiation of ^{1}H methyl resonance at δ 0.86 led to an enhancement of the resonance assigned as the H6 methine and the H2' methylene. Additionally, when the new resonance at δ 3.24 was irradiated, only the remaining methyl of the dimethylazabicyclohexane motif was significantly enhanced. With the stereo configuration of carbon 6 of the dimethylazabicyclohexane fixed in the S orientation, an energy-minimized three-dimensional structure of PF-07329265 (Supplemental Fig. 5) placed the remaining methyl at 2.6 Å from the C2-position methine (carbon 6 using Advanced Chemistry Development laboratory nomenclature). In this model, the new methylene is 3.8 Å from the C2-position methine. Based on this data, the structure of M1 (PF-07329265) is assigned as (1R,2S,5S,6S)-N-{(1S)-1-cyano-2-[(3S)-2-oxopyrrolidin-3-yl]ethyl}-6-(hydroxymethyl)-6-methyl-3-[3-methyl-N-(trifluoroacetyl)-L-valyl]-3-azabicyclo[3.1.0]hexane 2-carboxamide.

Metabolite M2

Metabolite M2 (PF-07329266) possessed a protonated molecular ion of m/z^+ 516.2441, which was consistent with a molecular formula of $C_{23}H_{33}N_5O_5F_3$ (2.5 ppm) and also suggested a monohydroxylation in nirmatrelvir. The CID spectrum possessed the same fragment ions as M1 (PF-07329265) but with differing abundances suggesting that, like M1, the hydroxylation has occurred on the 6,6-dimethyl-3-azabicyclo[3.1.0]hexane fused ring (Supplemental Fig. 6). The ^{1}H NMR spectrum of biosynthesized PF-07329266 indicated that only the methyl protons in the dimethylazabicyclohexane ring had changed significantly from the ones observed in similarly acquired spectra of nirmatrelvir (Supplemental Fig. 7). The ^{1}H methyl resonance observed at δ 0.86 was absent in the isolated material with a new resonance observed at δ 3.26,

which integrated to two protons. This data established that M2 (PF-073 29266) is a diastereomer of M1 (PF-07329265) at the C6-position whose structure is assigned as (1R,2S,5S,6R)-N-{(1S)-1-cyano-2-[(3S)-2-oxopyrrolidin-3-yl]ethyl}-6-(hydroxymethyl)-6 methyl-3-[3-methyl-N-(trifluoroacetyl)-L-valyl]-3-azabicyclo[3.1.0]hexane-2-carboxamide.

Metabolite M3

Metabolite M3 (PF-07329267) possessed a protonated molecular ion of m/z^+ 516.2268, consistent with a molecular formula of $C_{23}H_{33}N_5O_5F_3$ (3.8 ppm) and a monohydroxylated nirmatrelvir metabolite. The CID spectra of m/z 516 did not provide meaningful fragment ions for structural assignment; however, the HCD spectrum afforded m/z 237.0856 and 110.0968 as additional diagnostic fragment ions (Supplemental Fig. 8). The latter ion indicates that the azabicylohexane ring is unmodified. The former, m/z 237.0856, is consistent with azabicylohexane ring scission yielding an ion possessing the trifluoroacetyl and tert-butyl groups with a dehydrated hydroxyl group. This creates the possibilities of hydroxylation of the amide nitrogen of the trifluoroacetamide, the tert-butyl group, or the carbon connecting these two. The ^{1}H spectrum of biosynthesized PF-07329267 (Supplemental Fig. 9) indicated a change in the proton resonances of the tert-butyl methyl relative to those observed in similarly acquired spectra for nirmatrelvir. The tert-butyl resonance in nirmatrelvir displayed a chemical shift at δ 0.99, which integrated to nine hydrogen atoms. In the ^{1}H spectrum of PF-07329267, the resonance was now at δ 0.89 and integrated to a total of six hydrogen atoms. Additionally, the HSQC spectral data revealed the presence of a new inequivalent methylene pair of resonances at δ 3.14/3.53 corresponding to a carbon with a chemical shift of 68.5 (Supplemental Fig. 10). Based on these data, the structure of M3 (PF-07329267) is assigned as (1R,2S,5S)-N-{(1S)-1-cyano-2-[(3S)-2-oxopyrrolidin-3-yl]ethyl}-3-[4-hydroxy-3-methyl-N-(trifluoroacetyl)-L-valyl]-6,6-dimethyl-3-azabicyclo[3.1.0]hexane-2-carboxamide.

Metabolite M4

Metabolite M4 (PF-07329268) was the dominant oxidative metabolite of nirmatrelvir in liver microsomes and hepatocytes from animals and humans. PF-07329268 comprised two closely eluting interconverting diastereomers and possessed a protonated molecular ion of m/z^+ 516.2436, which was consistent with a molecular formula of $C_{23}H_{33}N_5O_5F_3$ (1.5 ppm), and indicated yet another monohydroxylation in nirmatrelvir. PF-07329268 underwent facile in-source dehydration to m/z 498.2327, and subsequent fragmentation was conducted on this major ion (Supplemental Fig. 11). The CID spectra of m/z 498 yielded a major ion of m/z 319.1636, which indicates that the azabicyclo[3.1.0]hexanyl-dimethyloxobutane-trifluoroacetamide portion was unmodified. The facile loss of water and the equilibrating diastereomers suggest, but do not prove, that the site of hydroxylation is on the C5-position of the pyrrolidinone ring. The ^{1}H spectrum of biosynthesized PF-07329268 (Supplemental Fig. 12) revealed that the resonances of the C22 methylene were absent. Moreover, the ^{1}H-^{13}C HSQC spectra of the isolated metabolite revealed the presence of a new ^{1}H methine resonance at δ 5.01, which correlated with a carbon atom at a chemical shift of δ 77.3 (Supplemental Fig. 13). Based on these data, M4 (PF-07329268) was assigned as (1R,2S,5S)-N-{(1S) 1-cyano-2-[(3R)-5-hydroxy-2-oxopyrrolidin-3-yl]ethyl}-6,6-dimethyl-3-[3-methyl-N-(trifluoroacetyl)-L-valyl]-3-azabicyclo[3.1.0]hexane-2-carboxamide.

Pharmacologic Activity of M4 (PF-07329268)

M4 (PF-07329268), the major in vitro oxidative metabolite of nirmatrelvir in animals and humans, was active against recombinant SARS-CoV-2 3CL^{pro} with a K$_i$ (inhibition constant) value (3 nM) comparable

to the one noted with nirmatrelvir (Owen et al., 2021). Moreover, PF-07329268 also repressed SARS-CoV-2 replication in epithelial Vero E6 cells (Boras et al., 2021). However, the corresponding EC_{50} for PF-07329268 in the cellular antiviral assay was relatively weaker than the one observed with the parent compound (PF-07329268 EC_{50} = 690 nM, PF-07321332 EC_{50} = 74.5 nM).

Metabolite m/z 498

A protonated molecular ion at m/z^{+} 498.2332 was observed, consistent with a molecular formula of $C_{23}H_{31}N_5O_4F_3$ (1.9 ppm). Although this might be considered an in-source dehydration product of a hydroxylated metabolite, the presence of a sodiated ion at m/z 520.2151 ($C_{23}H_{30}N_5O_4F_3Na$; 1.7 ppm) precludes this possibility and suggests that it is a dehydrogenated metabolite of nirmatrelvir. The fragments in CID and HCD spectra for this metabolite (Supplemental Fig. 14) are identical to those generated from fragmentation of the in-source dehydrated ion of m/z 498 of metabolite M4; therefore, it is likely that the dehydrogenation occurred on the pyrrolidinone ring. However, the exact site of the dehydrogenation was not clear.

HPLC-UV profile of nirmatrelvir (10 μM) incubations with a panel of major human recombinant enzymes revealed that only CYP3A4 and 3A5 (see Fig. 2) were able to recapitulate the metabolic pathways of nirmatrelvir observed in NADPH-supplemented HLMs and human hepatocytes.

Enzyme Kinetics and f_{CL} Determination for Nirmatrelvir Metabolism in HLMs

Enzyme kinetic parameters and unbound $CL_{int,app}$ values for the formation of M1 (PF-07329265), M2 (PF-07329266), M3 (PF-07329267), and M4 (PF-07329268) in NADPH-supplemented HLM incubations with nirmatrelvir (0.02–200 μM) are depicted in Table 2; associated kinetic data are presented graphically in Fig. 5; and corresponding Eadie-Hofstee plots are presented in Supplemental Fig. 15. Visual inspection of the Eadie-Hofstee plots suggested typical hyperbolic Michaelis-Menten kinetics for M1 and M4. Metabolite formation rates for M1 and M4 were fitted to a Michaelis-Menten model with resulting K_M and V_{max} values of 28.0 μM and 17.2 pmol/min per mg and 25.5 μM and 381 pmol/min per mg, respectively. Formation rates for M2 were best fitted to a 2-enzyme nonsaturable model in which the low affinity kinetic parameters could not be accurately defined with the nirmatrelvir concentration range tested, and therefore the secondary rate ($CL_{int(2)}$) of the low-affinity enzyme(s) was estimated by linear approximation. The K_M, V_{max}, and $CL_{int(2)}$ estimates for M2 were 24.0 μM, 9.79 pmol/min per mg, and 0.00508 μl/min per mg, respectively. M3 formation rate data were best fit to an allosteric sigmoidal model in which the estimated K_{half}, V_{max}, and Hill values were 31.0 μM, 15.2

pmol/min per mg, and 0.959, respectively. Based on these kinetic parameter estimates, the unbound $CL_{int,app}$ values for the formation of M1, M2, M3, and M4 were 0.654, 0.439, 0.522, and 15.9 μl/min per mg, respectively, yielding a summed unbound $CL_{int,app}$ of 17.5 μl/min per mg for the oxidative metabolism of nirmatrelvir to M1–M4. Based on the output of the metabolite identification work, the in vitro hepatic metabolism of nirmatrelvir can be assumed to be predominantly oxidative in HLMs, with an overall $f_{m,CYP450}$ of 1. The fractions of nirmatrelvir clearance (f_{CL}) representing formation of M1, M2, M3, and M4 were 0.037, 0.025, 0.030, and 0.91, respectively.

Contribution of CYP3A4/5 in the Oxidative Metabolism of Nirmatrelvir

Contributions by CYP3A4/5 to the metabolism of nirmatrelvir were examined using a multiple concentration CYP450 selective chemical inhibitor study design in HLMs (Fig. 6; Table 3). For all four metabolites, inhibition curves were best fit to a four-parameter inhibition model. In the presence of ketoconazole (0.001–10 μM), the formation of M1, M2, M3, and M4 was inhibited 95%, 96%, 98%, and 99%, respectively.

The relative contribution of CYP3A4 and CYP3A5 toward the oxidative metabolism of nirmatrelvir to M1–M4 was examined in HLMs from genotyped individuals expressing high (CYP3A5*1/*1) CYP3A5 enzyme in the presence or absence of nonselective CYP3A4/5 and selective CYP3A4 inhibitors ketoconazole and CYP3cide (Tseng et al., 2014), respectively (Table 4). Differences between the inhibitory effects of CYP3cide and ketoconazole for the formation of M1 (3.7%), M3 (3.0%), and M4 (12%) were not statistically significant using a one-way ANOVA with Bonferroni's multiple comparison test (α = 0.01). Assessment of the differential inhibitory effects on M2 formation rates was not possible due to concentrations below the limit of quantitation in the presence of both inhibitors. Because M2 represents a minor metabolic pathway (f_{CL} = 0.025), further studies were not conducted. In summary, no significant CYP3A5 contribution is expected to the overall metabolism of nirmatrelvir in CYP3A5*1/*1 individuals.

Assigned CYP450 f_m values for the oxidative metabolites of nirmatrelvir in HLMs, based on the combined results of nirmatrelvir enzyme kinetics and chemical inhibition studies, are presented in Table 3. After normalizing the contribution of CYP3A to the f_{CL} for each metabolic pathway, the fraction of M1, M2, M3, and M4 generated by CYP3A4 ($f_{m,CYP3A}$) was 0.036, 0.024, 0.029, and 0.90, respectively, with a combined CYP3A4 f_m of 0.99 and f_m related to other unassigned CYP450s of 0.01. Collectively, these results indicated that the major enzyme involved in the metabolism (f_m = 0.99) of nirmatrelvir in HLMs is CYP3A4.

TABLE 2

Enzyme kinetics and fractional clearance determination for the metabolism of nirmatrelvir in human liver microsomes

Data represent the mean of two replicates.

Model	PF-07329265 (M1) MM	PF-07329266 (M2) 2-enzyme MM[a]	PF-07329266 (M2) 2-enzyme MM[b]	PF-07329267 (M3) AS	PF-07329268 (M4) MM	Total
K_M (μM)	28.0	24.0	–	31.0	25.5	
V_{max} (pmol/min per mg)	17.2	9.79	–	15.2	381	
H	–	–	–	0.959	–	
$CL_{int,app,u}$[c] (μl/min per mg)	0.654	0.434	0.00541	0.522	15.9	17.5
f_{CL}[d]	0.037	0.025	0.030	0.030	0.91	1.00

AS, allosteric sigmoidal; H, Hill slope; MM, Michaelis-Menten.
[a]Highest affinity parameters reported.
[b]Low affinity linear approximation $CL_{int,app,u}$ reported.
[c]Protein adjusted microsomal free fraction = 0.940 for 0.3 mg/ml incubation protein concentration.
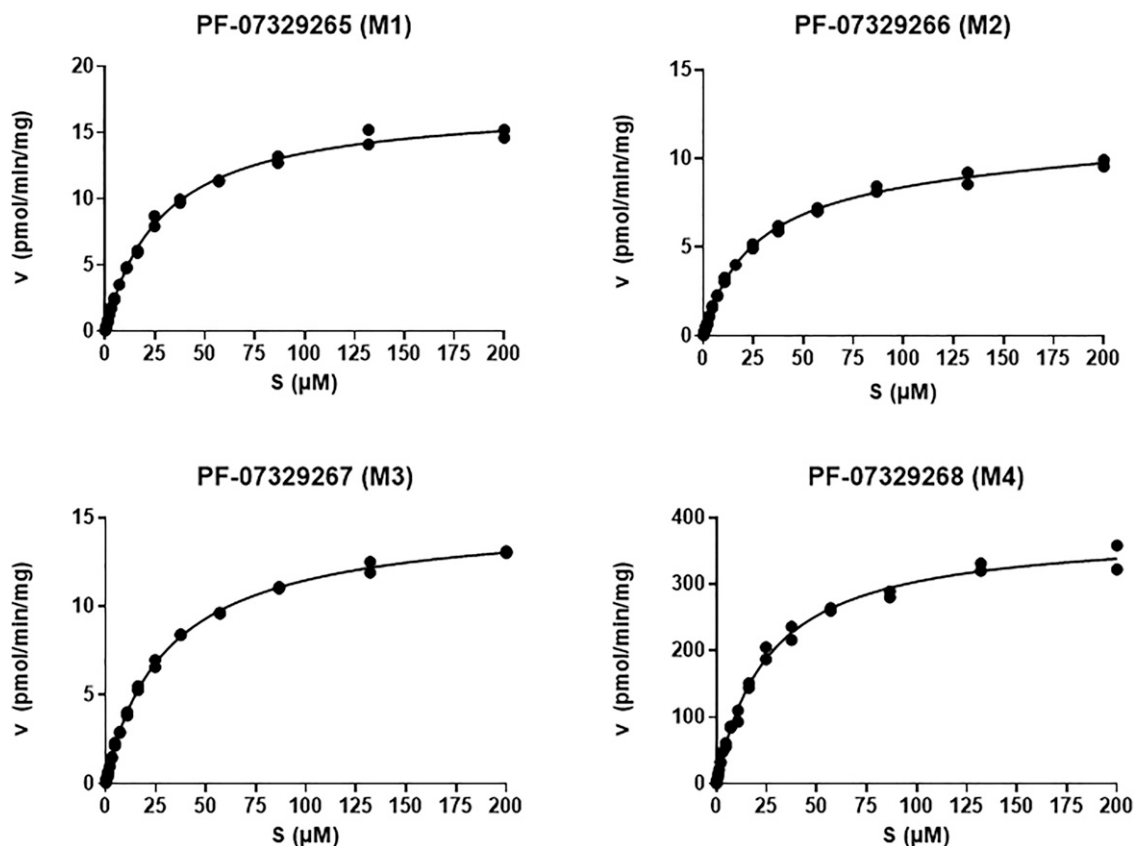[d]f_{CL} was calculated from eq. 7.

Fig. 5. Substrate saturation plots for the formation of the primary PF-07321332 (nirmatrelvir) metabolites PF-07329265 (M1), PF-07329266 (M2), PF-07329267 (M3), and PF-07329268 (M4) after incubation of PF-07321332 (0.02–200 μM) with HLMs (0.3 mg/ml).

Biliary Excretion of Unchanged Nirmatrelvir in SCHH

The potential for hepatobiliary excretion of nirmatrelvir in unchanged form was examined in SCHH. After a 10-minute incubation in SCHH, the corresponding $CL_{biliary,int,app}$ for nirmatrelvir (0.5 μM) in SCHH was 2.1 μl/min per mg, which was scaled using the methodology described by Kimoto et al. (2017) to yield a predicted human $CL_{biliary}$ of 2.7 ml/min per kg. The corresponding biliary excretion index of nirmatrelvir was ~43%. In comparison, positive control rosuvastatin (0.5 μM) (Kimoto et al., 2017) demonstrated $CL_{biliary,int,app}$ and biliary excretion index of 5.0 μl/min per mg and 52%, respectively.

PK of Nirmatrelvir in Animals

The PK parameters of nirmatrelvir after single intravenous and oral dose administration in rats and monkeys is shown in Table 5, and mean plasma concentrations versus time profile are shown in Supplemental Fig. 16. Nirmatrelvir (1 mg/kg) demonstrated moderate plasma clearance (CL_{plasma}) in rats (27.2 ml/min per kg) and monkeys (17.1 ml/min per kg) with low (0.33 l/kg in monkeys) to moderate (1.8 l/kg in rats) steady-state distribution volume (Vd_{ss}) values in the two species. The terminal $t_{1/2}$ ranged from 0.79 hours (monkeys) to 5.1 hours (rats). The percentage of unchanged nirmatrelvir excreted over a 24-hour period in rat and monkey urine was 17% and 7.0%, which yielded renal clearance (CL_{renal}) values of 4.5 and 1.3 ml/min per kg, respectively. The unbound renal blood clearance of nirmatrelvir in rats and monkeys, estimated using the protocol described by Dong et al. (2016), was 12 ml/min per kg and 4.0 ml/min per kg, respectively, and was within the range of the glomerular filtration rate in the respective species (rats = 8.7 ml/min per kg and monkeys = 4.0 ml/min per kg) (Lin, 1995),

suggesting little-to-no active tubular secretion. Consistent with these observations were the findings on the lack of substrate properties of nirmatrelvir toward a broad array of the major human renal transporters, including the organic anion transporters (OAT)1 and 3, multidrug and toxin extrusion protein (MATE)1 and 2K, organic cation transporter (OCT)2, and organic anion transporting polypeptide (OATP)4C1 (Pfizer data on file). After i.v. administration of nirmatrelvir (1 mg/kg) to bile-duct cannulated rats, 8.9% ± 4.7% of the administered dose was observed in rat bile in unchanged parent form, which translated to a $CL_{biliary}$ of 2.4 ml/min per kg. Comparison of the predicted CL_{hep} values using NADPH-supplemented liver microsomes and hepatocytes from rats and monkeys (Table 1) with the observed CL_{plasma} (after subtracting for CL_{renal} and $CL_{biliary}$) revealed a reasonably good (within ~2.5- to 5.0-fold in rats and within 2-fold in monkeys) in vitro-in vivo correlation for clearance.

Oral PK studies were conducted with two crystalline versions of nirmatrelvir: nirmatrelvir-MTBE cosolvate and anhydrous nirmatrelvir 'form 1.' After oral administration of nirmatrelvir (10 mg/kg) as MTBE cosolvate, nirmatrelvir was rapidly absorbed [T_{max} (time to reach C_{max}) = 0.25–1.5 hours] in rats and monkeys, with corresponding oral bioavailability (F) values of 50% and 8.5%, respectively. The corresponding fraction of the nirmatrelvir oral dose absorbed ($F_a \times F_g$) in rats and monkeys was 82% and 18%, respectively. The relatively lower F of nirmatrelvir in monkeys is likely due to CYP450-mediated oxidative metabolism along the gastrointestinal tract since nirmatrelvir demonstrated a facile metabolic decline ($t_{1/2}$ = 20.5 minutes, $CL_{int.app}$ = 33.8 μl/min per mg) in monkey intestinal microsomes in a NADPH-dependent fashion. This hypothesis is further substantiated by the
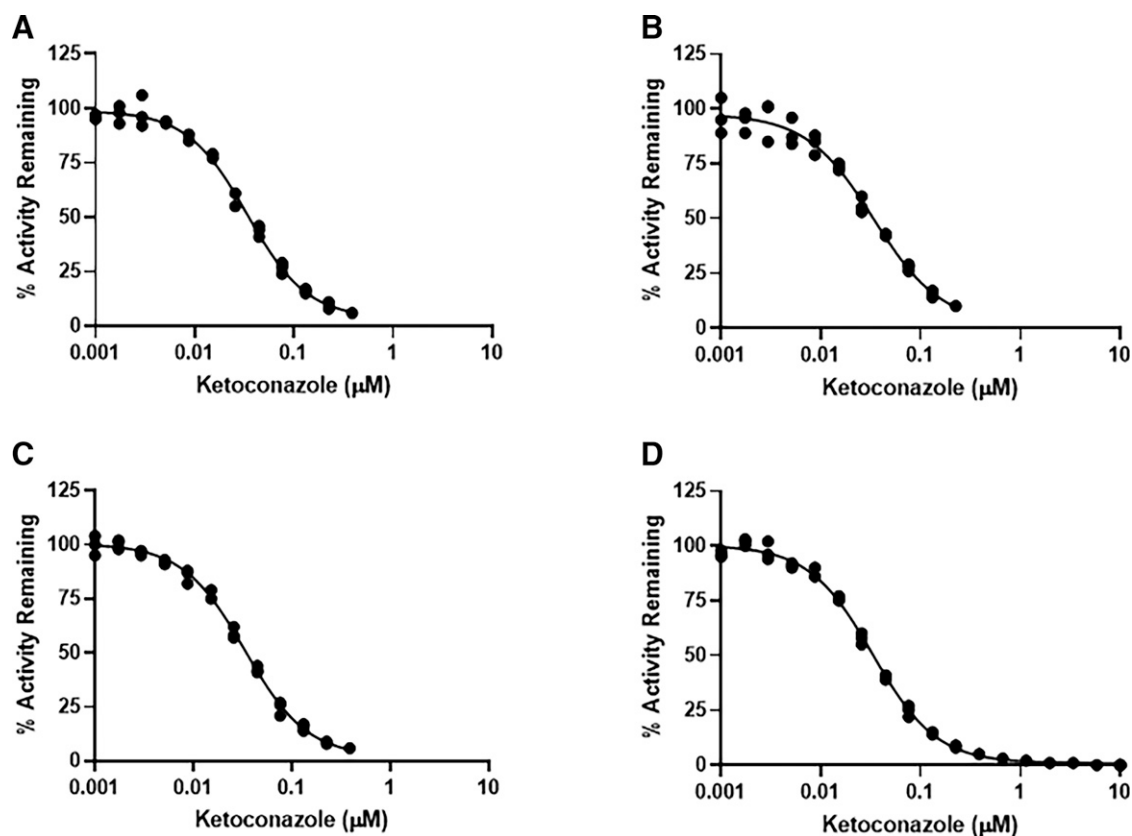
Fig. 6. Inhibition of the formation of M1–M4 metabolites of PF-07321332 (nirmatrelvir, 2.5 μM) in HLMs in the presence of the selective CYP3A inhibitor ketoconazole (0.001–10 μM), depicted in (A) PF-07329265 (M1), (B) PF-07329266 (M2), (C) PF-07329267 (M3), and (D) PF-07329268 (M4).

observation that unchanged nirmatrelvir constituted ∼4% of the administered dose in feces collected from monkeys after the oral dosing (data not shown). As such, nirmatrelvir did not demonstrate any metabolic turnover ($t_{1/2}$ > 240 minutes, $CL_{int,app}$ < 2.89 μl/min per mg) in rat and human intestinal microsomes in the presence of NADPH. Anhydrous nirmatrelvir 'form 1' orally administered (10 mg/kg) to rats also demonstrated rapid absorption (T_{max} = 0.25 hours), albeit with a lower F and lower $F_a \times F_g$ values of 34% ± 19% and 56% when compared with the anhydrous nirmatrelvir-MTBE cosolvate.

Interactions with Human CYP450 Enzymes

CYP450 Inhibition. Nirmatrelvir exhibited no reversible (IC_{50} > 100 μM) inhibition of CYP1A2 (phenacetin-O-dealkylation), CYP2B6

(bupropion hydroxylation), CYP2C8 (amodiaquine N-dealkylation), CYP2C9 (diclofenac-4'-hydroxylation), CYP2C19 (S-mephenytoin-4'-hydroxylation), and CYP2D6 (dextromethorphan-O-demethylation) catalytic activities in NADPH-supplemented HLMs. Nirmatrelvir, however, demonstrated weak reversible inhibition of CYP3A4/5 catalyzed testosterone-6β-hydroxylase, midazolam-1'-hydroxylase, and nifedipine oxidase activities with IC_{50} values of 58.3 μM, 106 μM, and 45.1 μM, respectively (Supplemental Table 4). An IC_{50} shift of 2.13× (midazolam-1'-hydroxylase) and 1.73× (testosterone-6β-hydroxylase) after a 30-minute preincubation of nirmatrelvir in NADPH-supplemented HLMs (Supplemental Table 4) suggested that nirmatrelvir is a reversible and time-dependent inhibitor of CYP3A enzyme activities. In the

TABLE 3

Assignment of fractional CYP450 contribution to the metabolism of nirmatrelvir in pooled HLMs

Data represent the mean of three replicates. Nirmatrelvir (2.5 μM) was incubated in pooled HLMs in the absence/presence of ketoconazole (0.001–10 μM).

Metabolic Pathway	Fraction of Clearance (f_{CL})	Fraction Inhibited[a]		Fraction Metabolized (f_m)[b]	
		CYP3A4	Unassigned[c]	CYP3A4	Unassigned
PF-07329265 (M1)	0.037	0.95	0.048	0.036	0.0018
PF-07329266 (M2)	0.025	0.96	0.043	0.024	0.0011
PF-07329267 (M3)	0.030	0.98	0.020	0.029	0.00058
PF-07329268 (M4)	0.91	0.99	0.0084	0.90	0.0077
Total	1.0			0.99	0.01

[a]The maximum contribution was determined by the percent activity remaining compared with a no inhibitor solvent control. Maximum percent inhibition was calculated using eq. 8.
[b]f_m = fraction metabolized calculated from:

$$f_{mMxCYPz} = \frac{\% \text{ inhibition}}{100} \times f_{CL} \quad (11)$$

[c]Other CYP450 isoforms unaccounted for, by inhibition with ketoconazole.

TABLE 4

Inhibition of nirmatrelvir (2.5 μM) metabolism in pooled HLMs with high (CYP3A5*1/*1) CYP3A5 activity

Data represent the mean of triplicate experiments. In cases where analyte concentrations were undetectable, the velocity was calculated using the lower limit of quantitation value.

HLM Lot	Inhibitor	CYP450	PF-07329265(M1) % Inhibition	PF-07329266(M2) % Inhibition	PF-07329267(M3) % Inhibition	PF-07329268(M4) % Inhibition
HLM 3A5*1/*1	Control	—	—	—	—	—
	Ketoconazole (1 μM)	3A4/5	98	>94	98	97
	CYP3cide (1 μM)	3A4	94	>94	95	85
	% Contribution CYP3A5		NS (3.7)	ND	NS (3.0)	NS (12)[a]

ND, not determined; NS, not significant (significance based on one-way ANOVA analysis with Bonferroni's multiple comparison test, $P < 0.01$).
[a]P value was 0.0294.

IC$_{50}$ shift assay, nirmatrelvir was devoid of time-dependent inhibition of CYP1A2, CYP2B6, CYP2C8, CYP2C9, CYP2C19, and CYP2D6 enzyme activities. Under the present experimental conditions, known CYP450 isozyme-specific reversible (and time-dependent) positive control inhibitors (Walsky and Obach, 2004) demonstrated potent reversible and time-dependent inhibition of CYP1A2, 2B6, 2C8, 2C9, 2C19, 2D6, and 3A activity, respectively, in NADPH-supplemented HLMs (Pfizer data on file).

Kinetics for the Time-Dependent Inhibition of CYP3A by Nirmatrelvir. Nirmatrelvir demonstrated time (1–40 minutes)- and concentration (0.1–100 μM)-dependent inhibition of the midazolam-1'-hydroxylase and testosterone-6β-hydroxylase activities in NADPH-supplemented HLMs (Fig. 7). Nirmatrelvir (100 μM) did not cause time-dependent inhibition (TDI) of CYP3A activity in HLM incubations in the absence of NADPH (see Fig. 7). The corresponding kinetic constants maximal rate of inactivation (k$_{inact}$) and inactivator concentration required to achieve 50% k$_{inact}$ (K$_I$) for TDI of the CYP3A catalyzed midazolam-1'-hydroxylase (and testosterone 6β-hydroxylase) activity by nirmatrelvir were 0.0142 minutes^{-1} (0.0165 minutes^{-1}) and 15.5 μM (13.9 μM), respectively. The ratio of k$_{inact}$/K$_I$ for the two marker substrates midazolam and testosterone was 0.916 ml/min per μmol and 1.23 ml/min per μmol, respectively (Supplemental Table 5). The rates of CYP3A

inactivation in HLMs with positive control verapamil (Walsky and Obach, 2004) were within historical results (Pfizer data on file).

Metabolic-Intermediate Complex Formation. The potential for quasi-irreversible inhibition of CYP3A4 by nirmatrelvir via the formation of a metabolic-intermediate (MI) complex (Orr et al., 2012) was examined in incubations of nirmatrelvir with NADPH-supplemented recombinant human CYP3A4 supersomes by monitoring the absorption spectra for the signature MI Soret absorbance at $\lambda \sim 455$ nm (Franklin, 1974). As shown in Supplementary Fig. 17, the absorbance at 455 nm did not increase after addition of NADPH to incubations of CYP3A4 supersomes and nirmatrelvir. In contrast, an expected increase in absorbance at 455 nm was observed in incubations of CYP3A4 supersomes/NADPH with the positive control troleandomycin, which is known to inactivate CYP3A4 via MI complex formation (Mayhew et al., 2000).

CYP450 Induction. The potential for induction of CYP3A4 messenger RNA (mRNA) and enzyme (midazolam-1'-hydroxylase) activity was examined in four lots (BXM, BNA, FOS, and HH1144) of cryopreserved human hepatocytes treated with nirmatrelvir (0.01–200 μM) for 48 hours. Nirmatrelvir demonstrated moderate induction of CYP3A mRNA levels and in a dose-dependent fashion in all four donor hepatocytes. Induction of CYP3A-mediated midazolam-1'-hydroxylase activity was seen in three out of the four lots. The maximal fold induction (IND$_{max}$) and inducer concentration required to achieve 50% IND$_{max}$

TABLE 5

Pharmacokinetics of nirmatrelvir in rats and monkeys

Species[a]	Dose (mg/kg)	C$_{max}$ (ng/ml)	T$_{max}$(h)	AUC$_{0-\infty}$(ng·h/ml)	CL$_{plasma}$(ml/min per kg)	Vd$_{ss}$(l/kg)	t$_{1/2}$(h)	Oral F (%)	F$_a$ × F$_g$ (%)[b]
Rat	1.0 (i.v.)	—	—	632 (523, 741)	27.2 (22.5, 31.9)	1.8 (1.4, 2.2)	5.1 (3.3, 7.0)	—	
	10 (oral)[c,d]	1290 (851, 1730)	1.5 (1.0, 2.0)	3190 (1890, 4480)	—	—	4.0 (2.9, 5.1)	50 (30, 71)	82
Monkey	10 (oral)[c,e]	1450 ± 373	0.25 ± 0.0	2170 ± 1180	—	—	2.8 ± 1.4	34 ± 19	56
	1.0 (i.v.)	—	—	977 (965, 988)	17.1 (16.9, 17.3)	0.33 (0.31, 0.34)	0.79 (0.74, 0.83)	—	
	10 (oral)[c,d]	1450 (1050, 1850)	0.25 (0.25, 0.25)	831 (747, 914)[f]	—	—	—	8.5 (7.7, 9.4)	18

Em dashes, not applicable; Vd$_{ss}$, steady-state distribution volume.
[a]Pharmacokinetic parameters were calculated from plasma concentration-time data and are reported as mean (± S.D. for $n = 3$ and individual values for $n = 2$). All pharmacokinetics were conducted in males of each species (Wistar-Han rats and cynomolgus monkeys). Intravenous (i.v.) doses for nirmatrelvir were administered as a solution in 10% DMSO/30% PEG400/60% deionized water (rats) or 5% (v/v) PEG400/95% (v/v) of 23% 2-hydroxypropyl-β-cyclodextrin in aqueous sodium phosphate buffer pH = 6.0 (monkeys).
[b]Fraction of the oral dose absorbed estimated from CL$_{plasma}$ after subtracting CL$_{renal}$. CL$_{plasma}$ was converted into CL$_{blood}$ by dividing CL$_{plasma}$ by the blood-to-plasma ratio in the respective species. Q is the hepatic blood flow (70 ml/min per kg in rats and 44 ml/min per kg in monkeys).
[c]Oral pharmacokinetic studies were conducted in the fed state. Oral rat pharmacokinetic studies were conducted with crystalline nirmatrelvir anhydrous MTBE solvate or anhydrous 'form 1.' Nirmatrelvir-MTBE solvate and anhydrous 'form 1' forms were formulated as solutions in 10% (v/v) ethanol/10% (v/v) Capmul MCM/35% (v/v) PEG400/45% (v/v) Tween80 and 2% (v/v) Tween80/98% of 0.5% (w/v) methyl cellulose in deionized water, respectively. Rats received 8 ml/kg orally of 1% hydroxypropyl cellulose in deionized water immediately prior to the nirmatrelvir-MTBE solvate oral dose. For oral pharmacokinetic assessments in monkeys, crystalline MTBE solvate form of nirmatrelvir was administered as a solution in 2% (v/v) Tween80/98% of 0.5% (w/v) methyl cellulose in deionized water.
[d]Nirmatrelvir was dosed as the anhydrous MTBE solvate.
[e]Nirmatrelvir was dosed as the anhydrous 'form 1.'
[f]AUC$_{0-t}$.

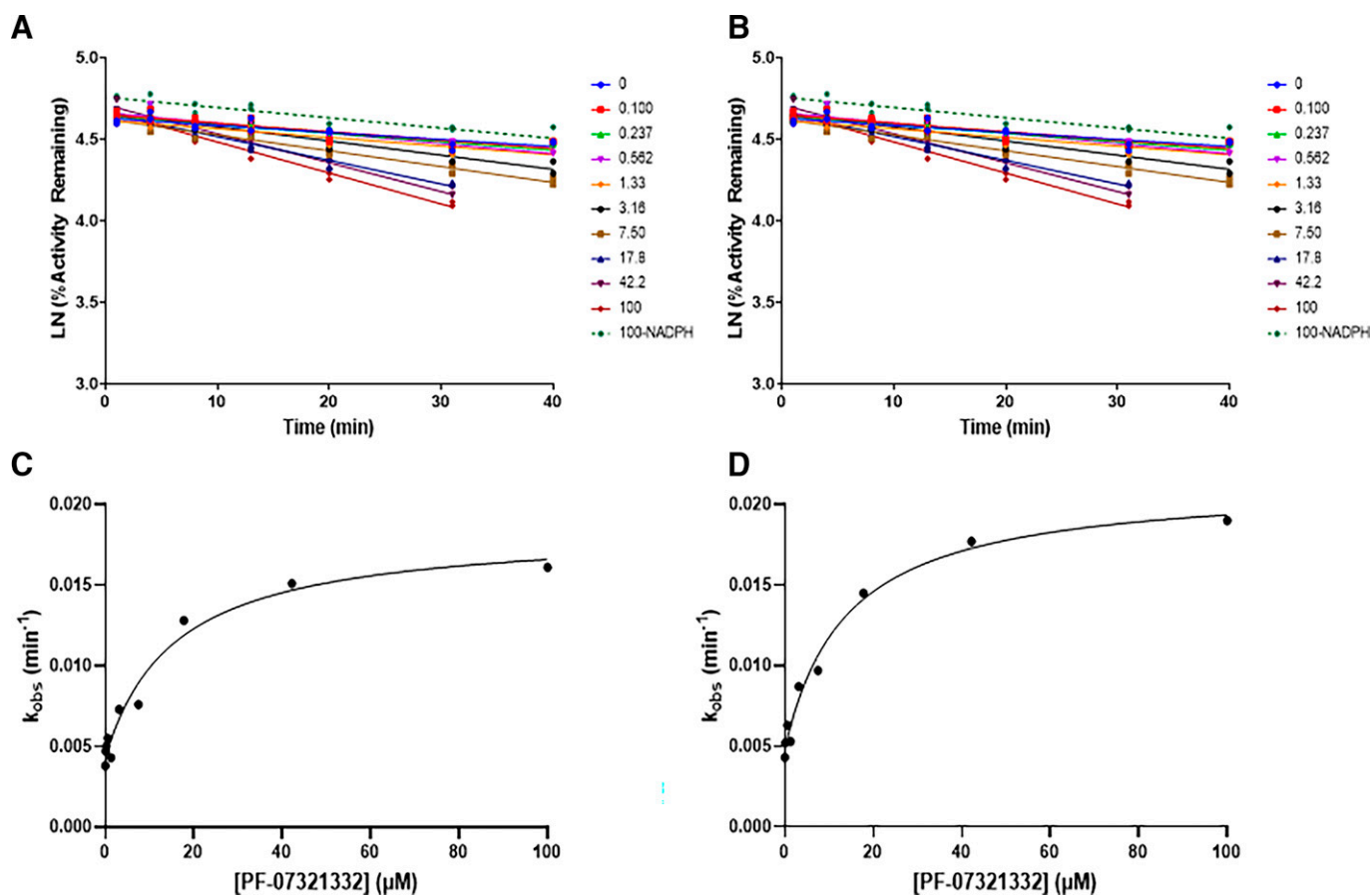$$F_a \times F_g = \frac{F}{1 - \frac{CL_{blood}}{Q}} \quad (12)$$

(12)

Fig. 7. Time-, concentration-, and NADPH-dependent inhibition of CYP3A4/5 catalyzed midazolam-1′-hydroxylase (A and C) and testosterone-6β-hydroxylase (B and D) activities in HLMs by PF-07321332 (nirmatrelvir). 100-NADPH = PF-07321332 (100 μM) incubations in HLMs in the absence of NADPH cofactor. (C) and (D) depict enzyme kinetics parameter fit (k_{obs} versus PF-07321332 concentrations) for midazolam and testosterone hydroxylation, respectively.

(EC_{50}) values for fold increases in CYP3A mRNA levels and midazolam-1'-hydroxylase activity in the four individual human hepatocytes with nirmatrelvir are shown in Supplemental Table 6. A cytotoxicity assay using Promega's CellTiter 96 aqueous nonradioactive cell proliferation assay kit (Promega, WI) showed no reduction in hepatocyte cell viability after treatment with nirmatrelvir at the tested concentrations. Under these experimental conditions, treatment of the four human donor hepatocyte lots with a single concentration (10 μM) of the positive control rifampicin led to the expected increases in CYP3A4 mRNA and catalytic activity. Moreover, rifampin demonstrated ∼2- to 3-fold greater increase in CYP3A mRNA and ∼2- to 5-fold greater increase in enzyme activity relative to the effects observed with nirmatrelvir at the higher end of its tested concentration range (50–200 μM).

Interactions with Human Drug Transporters

Inhibitory effects of nirmatrelvir against the major human intestinal, hepatobiliary, and renal drug transporters were examined using human embryonic kidney (HEK)293 cells or vesicles (Supplemental Table 7). Nirmatrelvir inhibited N-methylquinidine transport in human MDR1 expressing HEK293 vesicles with an IC_{50} value of 71 μM. Inhibition of rosuvastatin transport ($IC_{50} = 44$ μM) in OATP1B1 expressing HEK293 cells was also observed with nirmatrelvir. Relatively weaker inhibition ($IC_{50} > 100$ μM) by nirmatrelvir was noted against OATP1B3, the organic cation or anion transporters (OCT1, OCT2, OAT1, and OAT3), MATE1, and MATE2K.

Discussion

A major objective of our discovery campaign was to identify a compound(s) that had improved preclinical oral absorption relative to the intravenous agent PF-00835231 [oral bioavailability (oral F) and $F_a \times F_g = 1.4\%$ and 3.3% for rats, <0.05% and <1% for monkeys], while retaining the antiviral potency toward SARS-CoV-2 (Owen et al., 2021). The low oral absorption of PF-00835231 was largely attributed to a high hydrogen bond donor (HBD) count (Veber et al., 2002), which resulted in poor passive permeability (MDCK II $P_{app} < 0.27 \times 10^{-6}$ cm/s) across cells (Boras et al., 2021). Reduction in HBD count [PF-00835231 HBD = 5 → PF-07321332 (nirmatrelvir) HBD = 3] was achieved through the 3CL[pro] cocrystal structure-guided replacements of the P1' (α-hydroxymethyl ketone → nitrile), P2 (leucine → 6,6-dimethyl-3-azabicyclo[3.1.0]hexane as a cyclic leucine mimetic), and P3 (methoxyindole → trifluoroacetamide capping group) structural elements to yield a broad coronavirus inhibitor PF-07321332 (nirmatrelvir), which retained the potent inhibitory attributes of PF-00835231 toward SARS-CoV-2 3CL[pro] and possessed antiviral activity in cells and in a mouse-adapted SARS-CoV-2 model of COVID-19 (Owen et al., 2021). Nirmatrelvir also demonstrated panhuman coronavirus activity through inhibition of 3CL[pro] enzymes associated with alpha and betacoronaviruses capable of infecting humans (Owen et al., 2021). Lack of inhibitory effects toward several mammalian protease enzymes established the selectivity of nirmatrelvir as a coronavirus inhibitor.

A reduced HBD count also led to considerable improvements in oral absorption. Although nirmatrelvir demonstrated relatively low passive permeability and was an MDR1 substrate in vitro, oral administration of two crystalline forms (MTBE cosolvate and anhydrous 'form 1') of nirmatrelvir (10 mg/kg) to rats led to reasonable oral F (34%–50%), with the MTBE cosolvate demonstrating better absorption relative to the anhydrous 'form 1.' The superior oral absorption profile of the MTBE cosolvate presumably occurred because of its higher thermodynamic aqueous solubility and faster dissolution rate as compared with 'form 1.' The relatively poor bioavailability of MTBE cosolvate in monkeys was attributed to oxidative metabolism by CYP450 enzymes along the gastrointestinal tract, based on the monkey intestinal microsomal stability data. Nirmatrelvir was resistant to CYP450 oxidations in intestinal microsomal preparations from rats and humans, and moreover, complete resistance toward peptide backbone hydrolysis via the putative action of digestive enzymes was also noted in gastrointestinal fluids.

The low oral F (8.5%) of nirmatrelvir in monkeys did not deter toxicological investigations in this species (Owen et al., 2021). Daily dosing of nirmatrelvir-MTBE cosolvate (60–600 mg/kg) in 2-week regulatory toxicity studies led to robust increases in C_{max} and area under the plasma concentration-time curve (AUC) (Supplemental Table 8), most likely due to saturation or autoinhibition of first-pass oxidative metabolism in monkeys with increasing doses. Corresponding unbound systemic concentration (C_{max} and AUC) margins at the highest dose (600 mg/kg) were >200-fold over the measured unbound EC_{90} (181 nM) in the dNHBE assay. Rats orally administered with nirmatrelvir (40–1000 mg/kg) yielded unbound concentrations of $\sim$273-fold (C_{max}) and 65-fold (AUC) over the dNHBE unbound EC_{90} at the 1000 mg/kg dose (Owen et al., 2021). Nirmatrelvir was virtually devoid of any adverse findings at the highest doses tested in animals. It is noteworthy to point out that the SARS-CoV-2 dNHBE EC_{90} was also targeted as a minimally efficacious clinical concentration based on the observation that trough concentrations over cellular antiviral EC_{90} values are required for clinical efficacy with protease inhibitors and other antivirals (https://www.fda.gov/media/71223/download; Reddy et al., 2012). Improvements in oral absorption also permitted a thorough evaluation of the antiviral activity of nirmatrelvir in a mouse model of COVID-19. Twice-daily administration of nirmatrelvir (300 and 1000 mg/kg) in mice for 4 days protected the animals from weight loss and led to statistically significant reductions in viral load in the lungs of the infected animals with corresponding trough plasma concentrations maintained at $\sim$0.9-fold and 4.0-fold over the dNHBE EC_{90} (Owen et al., 2021).

The anticipated clearance mechanisms of nirmatrelvir in humans include oxidative metabolism, almost exclusively by CYP3A4, and some degree of renal and biliary excretion. In NADPH-supplemented HLMs and human hepatocytes, nirmatrelvir demonstrated moderate metabolic turnover to yield $CL_{int,app}$ values of 28.8 μl/min per mg and 5.16 μl/min per 10^6 cells, respectively, which were scaled to afford estimated CL_{hep} values of 6.3 and 3.2 ml/min per kg, respectively. Metabolic pathways of nirmatrelvir in liver microsomes and hepatocytes from animals and humans, comprising exclusively of CYP450 oxidation products, were virtually identical. The major metabolite M4, derived from pyrrolidinone ring oxidation in nirmatrelvir, demonstrated potent inhibition of recombinant SARS-CoV-2 3CL^{pro} activity but was relatively weaker as an antiviral agent in cells, potentially due to an impaired permeability, which was driven by the introduction of an additional HBD (OH group). Reaction phenotyping revealed that the selective CYP3A4/5 inhibitor ketoconazole inhibited the formation of the oxidative metabolites M1–M4 in HLMs by 95%–99%, with minimal contribution from CYP3A5 in pooled HLMs with high CYP3A5*1/*1 activity. Overall, this in vitro exercise, which established a preponderance of CYP3A4-mediated metabolism of nirmatrelvir, also created a

potential opportunity to enhance the therapeutic concentrations of nirmatrelvir in humans after concomitant administration with the CYP3A4 inhibitor ritonavir. Ritonavir is used as a PK booster of several marketed protease inhibitors such as darunavir and lopinavir that are predominantly metabolized by CYP3A4 (Cvetkovic and Goa, 2003; Mckeage et al., 2009; Larson et al., 2014).

Examination of inhibitory effects of nirmatrelvir toward major human CYP450 enzymes revealed inhibitory (reversible and time-dependent) and induction effects only against CYP3A. The mechanistic basis for the CYP3A TDI by nirmatrelvir is presently unclear and rules out a quasi-irreversible inhibitory pathway via MI complex formation as previously demonstrated with some peptidomimetics (Ernest et al., 2005). Projection of PK interactions through mechanistic modeling (https://www.fda.gov/media/134582/download) of the predicted human PK parameters and the in vitro CYP3A inhibition/induction data suggested that nirmatrelvir is likely to increase the AUC of drugs metabolized by CYP3A by 3.0- to 4.0-fold (Pfizer data on file). Moreover, regulatory guidance (https://www.ema.europa.eu/en/documents/scientific-guideline/guideline-investigation-drug-interactions-revision-1_en.pdf; https://www.fda.gov/media/134582/download) for assessing DDIs arising from inhibition of drug transporters also suggested the possibility of interactions between nirmatrelvir and drugs that are substrates for MDR1 and OATP1B1, based on the weak in vitro inhibitory effects noted for these transporters. Overall, the disposition attributes particularly the dominance of CYP3A-catalyzed oxidative metabolism over nonmetabolic elimination pathways, and the CYP3A4 inhibitory/inducing effects of nirmatrelvir are largely reminiscent of the profiles seen with marketed peptidomimetics, particularly ones (e.g., indinavir, darunavir, and lopinavir) used to treat acquired immunodeficiency syndrome (Lin et al., 1996; Kumar et al., 2004; Vermeir et al., 2009).

First-in-human pharmacokinetics of the crystalline anhydrous 'form 1' of nirmatrelvir administered as a single agent (150 mg) and in combination with ritonavir (nirmatrelvir 250 mg + ritonavir at −12, 0, and 12 hours) (study NCT04756531 on ClinicalTrials.gov) revealed a considerable enhancement in systemic concentrations of nirmatrelvir in the presence of ritonavir (Owen et al., 2021), which was consistent with the predominant role of CYP3A4 in nirmatrelvir metabolic clearance. The plasma concentrations of nirmatrelvir in the presence of ritonavir at 12 hours postdose were considerably greater than the SARS-CoV-2 antiviral EC_{90} value in dNHBE cells, which bolstered our confidence in attaining antiviral activity against pan-coronaviruses (Owen et al., 2021). Detailed data from the safety, tolerability, and clinical pharmacokinetics of nirmatrelvir and nirmatrelvir/ritonavir combination across single- and multiple-ascending doses have been recently submitted for publication (Singh, Toussi, Hackman, Chan, Rao, Allen, Van Eyck, Pawlak, Kadar, Clark, et al., 2022) . In a recent phase 2/3 trial (study NCT04960202 on ClinicalTrials.gov), the combination of nirmatrelvir/ritonavir (Paxlovid) demonstrated robust efficacy at reducing hospitalization and death in high-risk COVID-19 patients by 89% (within 3 days of symptom onset) and 88% (within 5 days of symptom onset) compared with placebo. Paxlovid has been recently granted emergency use authorization by multiple regulatory agencies around the globe, including the US Food and Drug Administration, for the treatment of mild-to-moderate COVID-19 in adults and pediatric patients (12 years of age and older) who are at high risk for progression to severe COVID-19, including hospitalization or death.

Authorship Contributions

Participated in research design: Obach, Di, Boras, Singh, Kalgutkar.

Conducted experiments: Eng, Dantonio, Kadar, Obach, Walker, Novak, Kimoto.

Contributed new reagents or analytic tools: Obach, Walker.

Performed data analysis: Eng, Dantonio, Kadar, Obach, Di, Lin, Patel, Boras, Walker, Novak, Kimoto, Singh.

Wrote or contributed to the writing of the manuscript: Eng, Dantonio, Kadar, Obach, Di, Patel, Boras, Walker, Kimoto, Singh, Kalgutkar.

References

Anand K, Ziebuhr J, Wadhwani P, Mesters JR, and Hilgenfeld R (2003) Coronavirus main proteinase (3CLpro) structure: basis for design of anti-SARS drugs. *Science* **300**:1763–1767.
Austin RP, Barton P, Cockroft SL, Wenlock MC, and Riley RJ (2002) The influence of nonspecific microsomal binding on apparent intrinsic clearance, and its prediction from physicochemical properties. *Drug Metab Dispos* **30**:1497–1503.
Bi YA, Kazolias D, and Duignan DB (2006) Use of cryopreserved human hepatocytes in sandwich culture to measure hepatobiliary transport. *Drug Metab Dispos* **34**:1658–1665.
Boras B, Jones RM, Anson BJ, Arenson D, Aschenbrenner L, Bakowski MA, Beutler N, Binder J, Chen E, Eng H, et al. (2021) Preclinical characterization of an intravenous coronavirus 3CL protease inhibitor for the potential treatment of COVID19. *Nat Commun* **12**:6055.
Cui J, Li F, and Shi ZL (2019) Origin and evolution of pathogenic coronaviruses. *Nat Rev Microbiol* **17**:181–192.
Cvetkovic RS and Goa KL (2003) Lopinavir/ritonavir: a review of its use in the management of HIV infection. *Drugs* **63**:769–802.
Di L, Keefer C, Scott DO, Strelevitz TJ, Chang G, Bi YA, Lai Y, Duckworth J, Fenner K, Troutman MD, et al. (2012) Mechanistic insights from comparing intrinsic clearance values between human liver microsomes and hepatocytes to guide drug design. *Eur J Med Chem* **57**:441–448.
Di L, Whitney-Pickett C, Umland JP, Zhang H, Zhang X, Gebhard DF, Lai Y, Federico 3rd JJ, Davidson RE, Smith R, et al. (2011) Development of a new permeability assay using low-efflux MDCKII cells. *J Pharm Sci* **100**:4974–4985.
Dong JQ, Varma MV, Wolford A, Ryder T, Di L, Feng B, Terra SG, Sagawa K, and Kalgutkar AS (2016) Pharmacokinetics and disposition of the thiouracil derivative PF-06282999, an orally bioavailable, irreversible inactivator of myeloperoxidase enzyme, across animals and humans. *Drug Metab Dispos* **44**:209–219.
Ernest 2nd CS, Hall SD, and Jones DR (2005) Mechanism-based inactivation of CYP3A by HIV protease inhibitors. *J Pharmacol Exp Ther* **312**:583–591.
Franklin MR (1974) The formation of a 455 nm complex during cytochrome P-450-dependent N-hydroxyamphetamine metabolism. *Mol Pharmacol* **10**:975–985.
Hoffman RL, Kania RS, Brothers MA, Davies JF, Ferre RA, Gajiwala KS, He M, Hogan RJ, Kozminski K, Li LY, et al. (2020) Discovery of ketone-based covalent inhibitors of coronavirus 3CL proteases for the potential therapeutic treatment of COVID-19. *J Med Chem* **63**:12725–12747.
Hu B, Guo H, Zhou P, and Shi ZL (2021) Characteristics of SARS-CoV-2 and COVID-19. *Nat Rev Microbiol* **19**:141–154.
Jin Z, Du X, Xu Y, Deng Y, Liu M, Zhao Y, Zhang B, Li X, Zhang L, Peng C, et al. (2020) Structure of Mpro from SARS-CoV-2 and discovery of its inhibitors. *Nature* **582**:289–293.

Kimoto E, Bi YA, Kosa RE, Tremaine LM, and Varma MVS (2017) Hepatobiliary clearance prediction: species scaling from monkey, dog, and rat, and in vitro-in vivo extrapolation of sandwich-cultured human hepatocytes using 17 drugs. *J Pharm Sci* **106**:2795–2804.
Kumar GN, Jayanti VK, Johnson MK, Uchic J, Thomas S, Lee RD, Grabowski BA, Sham HL, Kempf DJ, Denissen JF, et al. (2004) Metabolism and disposition of the HIV-1 protease inhibitor lopinavir (ABT-378) given in combination with ritonavir in rats, dogs, and humans. *Pharm Res* **21**:1622–1630.
Larson KB, Wang K, Delille C, Otofokun I, and Acosta EP (2014) Pharmacokinetic enhancers in HIV therapeutics. *Clin Pharmacokinet* **53**:865–872.
Lin J (1995) Species similarities and differences in pharmacokinetics. *Drug Metab Dispos* **23**:1008–1021.
Lin JH, Chiba M, Balani SK, Chen IW, Kwei GY, Vastag KJ, and Nishime JA (1996) Species differences in the pharmacokinetics and metabolism of indinavir, a potent human immunodeficiency virus protease inhibitor. *Drug Metab Dispos* **24**:1111–1120.
Lu R, Zhao X, Li J, Niu P, Yang B, Wu H, Wang W, Song H, Huang B, Zhu N, et al. (2020) Genomic characterisation and epidemiology of 2019 novel coronavirus: implications for virus origins and receptor binding. *Lancet* **395**:565–574.
Mayhew BS, Jones DR, and Hall SD (2000) An in vitro model for predicting in vivo inhibition of cytochrome P450 3A4 by metabolic intermediate complex formation. *Drug Metab Dispos* **28**:1031–1037.
McKeage K, Perry CM, and Keam SJ (2009) Darunavir: a review of its use in the management of HIV infection in adults. *Drugs* **69**:477–503.
Murdande SB, Pikal MJ, Shanker RM, and Bogner RH (2011) Aqueous solubility of crystalline and amorphous drugs: challenges in measurement. *Pharm Dev Technol* **16**:187–200.
Nagar S, Argikar UA, and Tweedie DJ (2014) Enzyme kinetics in drug metabolism: fundamentals and applications. *Methods Mol Biol* **1113**:1–6.
Orr ST, Ripp SL, Ballard TE, Henderson JL, Scott DO, Obach RS, Sun H, and Kalgutkar AS (2012) Mechanism-based inactivation (MBI) of cytochrome P450 enzymes: structure-activity relationships and discovery strategies to mitigate drug-drug interaction risks. *J Med Chem* **55**:4896–4933.
Owen DR, Allerton CMN, Anderson AS, Aschenbrenner L, Avery M, Berritt S, Boras B, Cardin RD, Carlo A, Coffman KJ, et al. (2021) An oral SARS-CoV-2 Mpro inhibitor clinical candidate for the treatment of COVID-19. *Science* **374**:1586–1593.
Pillaiyar T, Manickam M, Namasivayam V, Hayashi Y, and Jung SH (2016) an overview of severe acute respiratory syndrome-coronavirus (SARS-CoV) 3CL protease inhibitors: peptidomimetics and small molecule chemotherapy. *J Med Chem* **59**:6595–6628.
Reddy MB, Morcos PN, Le Pogam S, Ou Y, Frank K, Lave T, and Smith P (2012) Pharmacokinetic/pharmacodynamic predictors of clinical potency for hepatitis C virus nonnucleoside polymerase and protease inhibitors. *Antimicrob Agents Chemother* **56**:3144–3156.
Rut W, Groborz K, Zhang L, Sun X, Zmudzinski M, Pawlik B, Wang X, Jochmans D, Neyts J, Mlynarski W, et al. (2021) SARS-CoV-2 Mpro inhibitors and activity-based probes for patient-sample imaging. *Nat Chem Biol* **17**:222–228.
Smart AL, Gaisford S, and Basit AW (2014) Oral peptide and protein delivery: intestinal obstacles and commercial prospects. *Expert Opin Drug Deliv* **11**:1323–1335.
Tseng E, Walsky RL, Luzietti Jr RA, Harris JJ, Kosa RE, Goosen TC, Zientek MA, and Obach RS (2014) Relative contributions of cytochrome CYP3A4 versus CYP3A5 for CYP3A-cleared drugs assessed in vitro using a CYP3A4-selective inactivator (CYP3cide). *Drug Metab Dispos* **42**:1163–1173.
Veber DF, Johnson SR, Cheng HY, Smith BR, Ward KW, and Kopple KD (2002) Molecular properties that influence the oral bioavailability of drug candidates. *J Med Chem* **45**:2615–2623.
Vermeir M, Lachau-Durand S, Mannens G, Cuyckens F, van Hoof B, and Raoof A (2009) Absorption, metabolism, and excretion of darunavir, a new protease inhibitor, administered alone and with low-dose ritonavir in healthy subjects. *Drug Metab Dispos* **37**:809–820.
Walsky RL and Obach RS (2004) Validated assays for human cytochrome P450 activities. *Drug Metab Dispos* **32**:647–660.
Wang J, Yadav V, Smart AL, Tajiri S, and Basit AW (2015) Toward oral delivery of biopharmaceuticals: an assessment of the gastrointestinal stability of 17 peptide drugs. *Mol Pharm* **12**:966–973.
Yang H, Yang M, Ding Y, Liu Y, Lou Z, Zhou Z, Sun L, Mo L, Ye S, Pang H, et al. (2003) The crystal structures of severe acute respiratory syndrome virus main protease and its complex with an inhibitor. *Proc Natl Acad Sci USA* **100**:13190–13195.
Zhou P, Yang XL, Wang XG, Hu B, Zhang L, Zhang W, Si HR, Zhu Y, Li B, Huang CL, et al. (2020) A pneumonia outbreak associated with a new coronavirus of probable bat origin. *Nature* **579**:270–273.
Zhu N, Zhang D, Wang W, Li X, Yang B, Song J, Zhao X, Huang B, Shi W, Lu R, et al.; China Novel Coronavirus Investigating and Research Team (2020) A novel coronavirus from patients with pneumonia in China, 2019. *N Engl J Med* **382**:727–733.
Ziebuhr J, Heusipp G, and Siddell SG (1997) Biosynthesis, purification, and characterization of the human coronavirus 229E 3C-like proteinase. *J Virol* **71**:3992–3997.

Address correspondence to: Dr. Amit S. Kalgutkar, Pfizer Worldwide Research, Development, and Medical, 610 Main Street, Cambridge, MA 02139. E-mail: amit.kalgutkar@pfizer.com